Calibration strategies of PDC kinetic energy models and their application to the construction of hazard maps

Calibration strategies of PDC kinetic models: Implementation on two user-friendly programs (ECMapProb and BoxMapProb) and illustrative applications to El Misti (Peru), Merapi (Indonesia) and Campi Flegrei (Italy)

A. Aravena[1,2], R. Cioni[1], A. Bevilacqua[3], M. de' Michieli Vitturi[3], T. Esposti Ongaro[3], and A. Neri[3]

[1]Dipartimento di Scienze della Terra, Università di Firenze, Firenze, Italy.

[2]Laboratoire Magmas et Volcans, Université Clermont Auvergne, CNRS, IRD, OPGC, Clermont-Ferrand, France.

[3]Istituto Nazionale di Geofisica e Vulcanologia, Sezione di Pisa, Pisa, Italy.

Corresponding author: A. Aravena (alvaro.aravena@uca.fr)[1]

Keywords: Pyroclastic density currents, volcanic hazard assessment, numerical modeling, kinetic models, energy cone model, box model, branching formulation.

Highlights

- We present a set of structured and reproducible strategies to calibrate PDC kinetic models.
- We implement these calibration strategies on two user-friendly programs: ECMapProb and BoxMapProb.
- These calibration strategies reduce the biases derived from arbitrary user choices in the construction of hazard maps.

Abstract

[1] **Authorship statement**
All co-authors contributed in the manuscript preparation and the identification of the study cases presented in this paper. AA programmed the models ECMapProb and BoxMapProb, run simulations and post-processed results. AA, AB, MdMV and TEO worked in the mathematical description of the models and the calibration strategies.

The availability of computer tools able to describe the behavior of pyroclastic density currents (PDCs) with uncertainty quantification is of primary importance for the assessment of volcanic hazard. A common strategy to assess the intrinsic variability of these phenomena is based on the analysis of large sets of numerical simulations with variable input parameters. The use of models fast enough to allow for a large number of simulations, such as the so-called kinetic models, is thus needed. However, due to the sensitivity of kinetic models on poorly constrained input parameters, the definition of their variation ranges is a critical step in the construction of hazard maps and a numerical calibration becomes necessary. In this work we present a set of reproducible and structured calibration procedures of kinetic models based either on a reference PDC deposit or on the distribution of runout distances or inundation areas of a number of documented PDCs. In the first case, various metrics can be adopted to compare the numerical results with the reference PDC deposit (Root mean square distance, Hausdorff distance and Jaccard index), facilitating the development of scenario-based hazard assessments. On the contrary, calibrations based on the distribution of runout distances or inundation areas allow constructing probabilistic hazard maps that are not conditioned on the occurrence of a specific scenario, but rather reflect the variability of the documented PDCs during the time window considered. Importantly, our calibration strategies allow setting the kinetic models input parameters considering their eventual interdependence. These procedures are implemented on improved, user-friendly versions of the programs ECMapProb and BoxMapProb, whose functionalities are presented for the first time in this paper. The different calibration strategies and the functionalities of our programs are illustrated by considering three case studies: El Misti (Peru), Merapi (Indonesia) and Campi Flegrei (Italy).

1. Introduction

Pyroclastic density currents (PDCs) are mixtures of pyroclasts, lithic fragments and gas typically produced by a lateral blast or by the collapse of an eruptive column or a volcanic dome (Druitt, 1998; Roche et al., 2013; Dufek et al., 2015; Lube et al., 2020). These flows are denser than the surrounding atmosphere and propagate laterally due to the effect of gravity, being strongly influenced by the volcano topography. PDCs represent one of the major hazards associated with volcanic systems, which have been systematically assessed by adopting an approach based on numerical modeling (Malin and Sheridan, 1982; Neri et al., 2003; Sheridan et al., 2004; Patra et al., 2005; Kelfoun et al., 2009; Doyle et al., 2010; Esposti Ongaro et al., 2011; 2016; Kelfoun, 2011; de' Michieli Vitturi et al., 2019; Aravena et al., 2020). PDCs pose important modeling challenges because of their complex propagation dynamics and the uncertainty in their initial conditions. Due to this uncertainty in the characteristics of future PDCs, a common strategy to assess the intrinsic variability of these phenomena is based on the analysis of a large number of simulations (e.g. 10^4-10^6) with variable input parameters (Neri et al., 2015; Tierz et al., 2016a; Bevilacqua et al., 2017; Rutarindwa et al., 2019; Patra et al., 2020). Consequently, the use of tools fast enough to allow for large numbers of simulations, such as the so-called kinetic models (e.g. energy cone and box model), is required, enabling the quick production of statistically robust hazard maps without an excessive computational expense. However, because of the sensitivity of kinetic models on the often poorly constrained input parameters, the definition of their variation ranges is a critical step in the construction of hazard maps.

The absence of common strategies to set the input parameters of kinetic models often limits the capability to perform comparative analyses between the results derived from different studies and models. Inter-comparison of models is in fact a critical step in the validation of numerical tools, as discussed by Esposti Ongaro et al. (2020a), being particularly relevant when these tools are used to define measures of volcanic risk mitigation. We stress that there are similar difficulties in any numerical model when it is adopted to describe a physical phenomenon characterized by significant uncertainty (Scollo et al., 2008; Worni et al., 2012; Biass et al., 2016; de' Michieli Vitturi and Tarquini, 2018; Bevilacqua et al., 2019; Yang et al., 2020), which appeals to the development of strategies to address this issue.

In this context, we present and apply to different case studies a set of reproducible and structured procedures to calibrate the input parameters of kinetic models based on geological information of the volcanic system of interest. These calibration strategies allow the reduction of the biases derived from arbitrary user assumptions in the construction of PDC hazard maps, which are often necessary due to lack of specific data. The geological information used in these calibration strategies can be described in terms of the inundation zone of a specific PDC or the distribution of runout distances or inundation areas of past PDCs. Importantly, these calibration procedures are implemented in the user-friendly programs ECMapProb and BoxMapProb, which are based on the branching and traditional formulations of the energy cone and the box model, respectively (Aravena et al., 2020), and whose functionalities and user manuals are presented for the first time in this paper (see Supplementary Material).

This study acknowledges and aims at complementing many previous efforts to set the input parameters of numerical models based on the eruptive record of volcanoes (e.g. Neri et al., 2015; Tierz et al., 2016a; 2016b; Ogburn and Calder, 2017; Cioni et al., 2020). We remark that the purpose of this work is not to compare the suitability of different calibration procedures or provide new hazard maps for well-documented volcanoes, but to present a set of calibration strategies that can be used for the quick construction of PDC inundation probabilistic maps and describe the functionalities of the programs ECMapProb and BoxMapProb. We illustrate these calibration strategies by considering three volcanic systems: El Misti (Peru), Merapi (Indonesia) and Campi Flegrei (Italy).

This paper consists of five sections. In Section 2 we describe briefly the numerical models used in this work and their input parameters. In Section 3 we present a set of reproducible calibration strategies of the inputs of kinetic models. In Section 4 we show three illustrative applications of our calibration strategies and, finally, in Section 5 we present a summary and the conclusion of this paper.

1.1 Setting the Input parameters of kinetic models: historical background

In the case of the energy cone model, where input parameters are collapse position ($Q_{0,0}$), collapse height ($H_{0,0}$, hereafter defined with respect to the topography) and the energy cone slope ($\tan(\varphi)$), several efforts have been devoted to constrain $\tan(\varphi)$ (Hsu, 1975). Sheridan and Macías (1995) studied the deposits of pyroclastic flows at Colima volcano (Mexico) showing that $\tan(\varphi)$ is influenced by the pyroclastic flow size. Hayashi and Self (1992) also found a negative correlation between $\tan(\varphi)$ and flow volume. The statistical correlation between flow volume and $\tan(\varphi)$ was further investigated and quantified in Spiller et al. (2014) and Ogburn et al. (2016). These papers have allowed constraining only partially the expected variability of $\tan(\varphi)$, and thus additional assumptions are needed to set this input parameter. Regarding the parameter $H_{0,0}$, it is worth noting that numerical simulations of 3D multiphase flow models (e.g. Esposti Ongaro et al., 2020b) have shown that column collapse height is virtually irrelevant in the determination of the flow runout. This is consistent with fieldwork evidence (Tadini et al., 2021) and results derived from integral inertial models. Consequently, the common interpretation of $H_{0,0}$ as a measure of the collapse height may be misleading in PDCs derived from collapsing columns, and thus $H_{0,0}$ has to be considered as a model parameter for which a numerical calibration becomes necessary.

In practice, to deal with the problem of setting the input parameters of the energy cone model, many strategies have been applied during the last decades, and the use of vent opening maps is not uncommon. For instance, Alberico et al. (2002) adopted the energy cone model to study PDC propagation at Campi Flegrei (Italy) using a vent opening probability map to define a set of likely collapse positions. In these simulations, input parameters were arbitrarily imposed defining two scenarios that roughly reflect the typical runout distance of small and large-scale PDCs in this volcanic system. Other examples where $H_{0,0}$ and $\tan(\varphi)$ were imposed deterministically are Macías et al. (2008) and Ferrés et al. (2013). Among the examples where a Monte Carlo strategy was used to sample input parameters, it is worth mentioning Tierz et al. (2016b), who performed an analysis of the inundation area and runout distance of past PDCs at Vesuvius and Campi Flegrei, and defined independent probability distributions for the inputs of the energy cone model. Other examples where a Monte Carlo approach was applied are Sandri et al. (2018) and Clarke et al. (2020).

Regarding the definition of the box model input parameters, it is worth citing Neri et al. (2015), who studied the geological record of Campi Flegrei to define probability distributions of the inundation area of past PDCs and then they used these data to compute the input conditions (in particular, the flow volume) of a set of simulations through an iterative method of numerical inversion (Bevilacqua, 2016). In addition, Neri et al. (2015) used the vent opening probability maps from Bevilacqua et al. (2015) for the construction of fully probabilistic maps of PDC inundation at Campi Flegrei. Their findings were further extended by Bevilacqua et al. (2017), who detailed the joint effects of vent position, PDC scale, and temporal eruption rates. In summary, both Neri et al. (2015) and Bevilacqua et al. (2017) considered the inundation area as a random variable whose definition is based on the vent location and the geological record of Campi Flegrei, which was therefore used as an input in the box model simulations performed. On the other hand, Tadini et al. (2021) constrained the input parameters of the box model for two significantly different PDC units of the AD 79 Vesuvius eruption, focusing on the average reconstruction of deposit thickness (Cioni et al., 2020) as a function of the distance from the collapse location.

2. Input parameters of the models

In this section, we briefly describe the input parameters of the traditional and branching formulations of the energy cone and the box model to frame the presentation of our calibration strategies. Further details of these models are presented in Huppert and Simpson (1980), Malin and Sheridan (1982), Sheridan and Malin (1983), Esposti Ongaro et al. (2016), Aravena et al. (2020) and in references therein.

2.1 Energy cone model

The energy cone model is a simple and widely used formulation to study PDC dispersal (Malin and Sheridan, 1982; Sheridan and Malin, 1983; Wadge and Isaacs, 1988). This model describes the evolution of the kinetic energy of a frictional flow by considering a constant rate of energy dissipation, which is compared with the potential energy needed to overcome the topographic obstacles the PDC faces. Consequently, this model suites to dense, frictional granular flows (Campbell, 2006; Pudasaini and Domnik, 2009). In addition to the collapse position $Q_{0,0}$, the input parameters of this model are: (a) collapse height ($H_{0,0}$), and (b) energy cone slope

($\tan(\varphi) = H/L$, where H represents the height difference between the collapse point and the position of maximum runout and L is the distance travelled by the PDC). These parameters allow defining a vertical-axis cone whose interaction with the topography gives rise to an inundation area, as shown in Figure 1a-b. Because this model does not consider processes of pyroclasts channelization, an enhanced formulation was presented by Aravena et al. (2020), where a *root* energy cone is complemented with *branch* energy cones in the preferential channelization directions of pyroclastic material. *Root* and *branch* energy cones are organized in a tree-like structure that gives rise to a branching structure (Harris, 1963; Asmussen and Hering, 1983; Haccou et al., 2005), which is stopped when the *branch* energy cones are not able to increase the inundation zone of the modeled PDC (in Figure 1 we illustrate graphically how an iterative procedure is able to increase the inundation area and channelize pyroclastic material). Importantly, the branching formulation does not add new, unconstrained input parameters and thus the calibration procedures described below are valid both for the traditional and the branching formulations.

2.2 Box model

The box model integral formulation, based on the pioneering work of Huppert and Simpson (1980), allows to describe inertial flows such as dilute PDCs (particle concentration of the order of 10^{-2} or less) and low aspect ratio ignimbrite-forming flows (Walker, 1983). In this model, friction is assumed to be negligible and the flow propagation dynamics is controlled by the hydrostatic pressure contrast and by the momentum dissipation due to particle sedimentation. The input parameters of the box model (Esposti Ongaro et al., 2016) are: (a) collapsing volume (V_0), (b) initial concentration of solid particles (ϕ_0), (c) Froude number (Fr), (d) sedimentation velocity (w_s); (e) solid particles density (ρ_p), and (f) ambient gas density (ρ_a). These parameters allow defining a vertical-axis conoid centered at the source position that is compared with the topography in order to calculate the inundation area. In this case as well, a new formulation based on the construction of additional (or *branch*) conoids in the zones of preferential channelization was presented by Aravena et al. (2020), which permits to improve the ability of the box model to reproduce channelization processes of pyroclastic material. The branching formulation does not involve the inclusion of additional input parameters and thus the calibration strategies described in this work are valid both for the traditional and the branching formulations of the box model.

3. Calibration strategies

Calibrating the input parameters of kinetic models is a critical step when they are used in the construction of PDC inundation probability maps, even if the Monte Carlo approach is adopted to sample the model inputs. This is because inundation probability maps are not only controlled by the variation range of the input parameters but also by their relative weights within the total number of simulations. In fact, the *probabilistic* nature of hazard maps computed from the invasion frequency within a set of numerical simulations is highly debatable if well-suited calibration procedures are not considered for their construction. For instance, Hyman et al. (2019) showed that selecting a non-uniform distribution over the input range can significantly enhance the robustness of numerical results.

In this section, we describe different strategies to calibrate the input parameters of kinetic models. To provide a common nomenclature, the calibrated input parameters are named α and β. For the energy cone model, α is defined as the collapse height ($H_{0,0}$) and β represents the energy cone slope ($\tan(\varphi)$). Instead, for the box model, α represents $\log(V_0)$ (with V_0 representing the collapsing volume) and β is defined as the initial particle concentration (ϕ_0). The other input parameters of the box model, whose expected variability typically exerts a lower influence on numerical results, are fixed. In any case, note that the six inputs of the box model are combined to define only two intermediate variables (L_{max} and C; see Aravena et al., 2020) which fully set the characteristics of the box model conoids. Thus, a calibration based on only two variable parameters is enough to capture the variability in the numerical results of this model. To develop a reproducible calibration procedure, we need to define a similarity index (S) between the results of a set of calibration simulations and a reference scenario or set of reference scenarios. In this work and in the programs ECMapProb and BoxMapProb, the latter can be defined in terms of a reference inundation polygon or a reference probability distribution of runout distance or inundation area.

Let consider a set of $N \times N$ calibration simulations with fixed source position and the input parameters variable within the cross product of predefined ranges ($\alpha \in [\alpha_1, \ldots, \alpha_N]$ and $\beta \in [\beta_1, \ldots, \beta_N]$). Both sequences of inputs are increasing and their values equidistant. We name $\mathrm{S}_{m,n}$ the similarity index between the modeled inundation polygon associated with the m-th value of α and the n-th value of β and the reference scenario or set of reference scenarios. $\mathrm{S}_{m,n}$ is assumed to be a non-negative number that increases as the consistency between the modeled inundation polygon and the reference scenario or set of reference scenarios increases. Thus, we can suppose that the ability of the pair of inputs (α_m, β_n) to describe well the reference scenario or set of reference scenarios is an increasing function of $\mathrm{S}_{m,n}$. This translates into a mathematical relationship between $\mathrm{S}_{m,n}$ and the sampling probability of a pair of inputs in the neighborhood of (α_m, β_n):

$$P\big((\alpha,\beta)\approx(\alpha_m,\beta_n)\big) := c_p \cdot \mathrm{S}_{m,n}^{\gamma} \tag{1}$$

where c_p is a proportionality constant and γ is a positive exponent. In our calibration strategies, for metrics based on a reference inundation polygon (see Section 3.1), we assume a second-order relationship ($\gamma = 2$) to enhance the weight of the pairs of input parameters with high values of $\mathrm{S}_{m,n}$ in the calibration simulations. Otherwise, for metrics based on a reference probability distribution of runout distance or inundation area (see Section 3.2), a first-order relationship is considered ($\gamma = 1$) in order to reproduce the predefined distribution of runout distance or inundation area.

Considering known values for $\mathrm{S}_{m,n}$ we can define a probability function for sampling the model inputs based on the reference scenario or set of reference scenarios. In practice, this means that we can calculate c_p by assuming:

$$\begin{cases} P(\alpha \in [\alpha_1, \alpha_N]) = 1 \\ P(\beta \in [\beta_1, \beta_N]) = 1 \end{cases} \tag{2}$$

In this work we describe five different similarity indexes, which are already implemented in the programs ECMapProb and BoxMapProb. Three approaches are based on a reference inundation polygon (i.e. the footprint over the topography of the inundation area of a given PDC; Section 3.1), and the other two approaches are based on predefined probability distributions of runout distance and inundation area, respectively (Section 3.2). These probability distributions are expected to be based on the geological record of the studied volcano.

Importantly, all the calibration strategies described in this work consider a possible statistical dependence between the model inputs. For instance, in the case of the energy cone model, the well-known relationship between PDC volume and $\tan(\varphi)$ likely translates into a mathematical relationship between $H_{0,0}$ and $\tan(\varphi)$ (see Section 4.1), which would imply that the input parameters cannot be sampled independently for the construction of PDC hazard maps. On the other hand, in the case of the box model, the product between V_0 and ϕ_0 represents the collapsing volume of pyroclasts, and thus the applicability of an independent sampling is highly debatable (see Section 4.3).

3.1 Metrics based on a reference inundation polygon

Let consider two inundation polygons (A and B) defined by the sets of boundary points A_i and B_j, respectively ($i = 1, \ldots, n_a$ and $j = 1, \ldots, n_b$). Polygon A is given by the reference inundation area (defined by the user in the programs ECMapProb and BoxMapProb) and polygon B is associated with a given calibration simulation (computed using $\alpha = \alpha_m$ and $\beta = \beta_n$). In our programs, in order to reduce the numerical errors derived from the definition of these polygons and to balance the weight given to the different portions of the polygons, their contour points are re-sampled considering a large number ($n_r = 1{,}000$) of equidistant points (with respect to the arc length) named A_k and B_k ($k = 1, \ldots, n_r$). Below we describe the three different metrics available to calculate $S_{m,n}$ based on a reference inundation polygon (Fig. 2).

3.1.1 Root mean square distance (RMSD)

This similarity index is based on the root mean square distance between the boundary points of each polygon (A_k and B_k) and the closest boundary point of the other one (Fig. 2a), i.e.:

$$RMSD_{m,n} := \frac{\sqrt{\left(\sum_{i=1}^{n_r}\left(\min_{j\,\in\,[1,n_r]}\left(d\left(A_i, B_j\right)\right)^2\right)\right) + \left(\sum_{i=1}^{n_r}\left(\min_{j\,\in\,[1,n_r]}\left(d\left(B_i, A_j\right)\right)^2\right)\right)}}{2n_r} \qquad (3)$$

where $RMSD$ is the matrix array containing the results of root mean square distance in the calibration simulations and the subscripts refer to the indices of this matrix. The lower the value of $RMSD_{m,n}$, the higher the similarity degree between the inundation polygons. From these results, the similarity index is:

$$S_{m,n}^{(1)} := \frac{1}{RMSD_{m,n} + \varepsilon_{DEM}} \tag{4}$$

where ε_{DEM} is the cell size of the DEM used in the calibration simulations, representing a measure of the DEM resolution-derived uncertainty in the calculation of the distance-based similarity metrics. We found that the effect of ε_{DEM} was negligible in all the tested cases, but it is still incorporated in Eq. 4 to avoid division by zero in any simulation condition (note that the minimum value computed for $RMSD_{m,n}$ in the studied cases is much larger than $\varepsilon_{DEM} \approx 30$ m).

3.1.2 Hausdorff distance (HD)

The second similarity index is defined by (Fig. 2b):

$$HD_{m,n} := \max\left\{ \max_{i \in [1,n_r]} \min_{j \in [1,n_r]} d(A_i, B_j),\ \max_{i \in [1,n_r]} \min_{j \in [1,n_r]} d(B_i, A_j) \right\} \tag{5}$$

where HD is the matrix array containing the Hausdorff distances associated with the calibration simulations and the subscripts refer to the indices of this matrix. The resulting similarity index is:

$$S_{m,n}^{(2)} := \frac{1}{HD_{m,n} + \varepsilon_{DEM}} \tag{6}$$

where ε_{DEM} is incorporated to avoid division by zero in any simulation condition.

3.1.3 Jaccard index (JI)

This similarity index compares the areas defined by the inundation polygons, and is given by (Fig. 2c):

$$JI_{m,n} = \frac{|A \cap B|}{|A \cup B|} \tag{7}$$

where JI is the matrix array containing the results of Jaccard index associated with the calibration simulations and the subscripts refer to the indices of this matrix. The Jaccard index ranges between 0 and 1, and is considered equal to the derived similarity degree (i.e., $S_{m,n}^{(3)} := JI_{m,n}$).

3.2 Metrics based on a reference probability distribution of runout distance or inundation area

3.2.1 Runout distance-based calibration

Since in some cases likely eruption scenarios have been defined by adopting the expected runout distance (e.g. Ferrés et al., 2013), we consider this parameter as a measure potentially useful to calibrate the inputs of kinetic models. In this case, no reference inundation polygon is needed and calibration is only based on a predefined distribution of runout distances. If F_{RD} is the cumulative distribution function of runout distance, we can compute a measure of the weight that must be assigned to a calibration simulation characterized by a runout distance $RD_{m,n}$ in order to reproduce the predefined distribution of runout distance:

$$S_{m,n}^{(4)} := \int_0^1 \frac{\left(\left|RD_{m,n} - F_{RD}^{-1}(x)\right| + \varepsilon_{DEM}\right)^{-1}}{\sum_{a=1}^{N}\sum_{b=1}^{N}\left(\left|RD_{a,b} - F_{RD}^{-1}(x)\right| + \varepsilon_{DEM}\right)^{-1}} dx \tag{8}$$

where RD is the matrix array containing the runout distances of the calibration simulations, and the subscripts indicate the indices of this matrix. Let consider a specific integration step defined by the cumulative probability x_s and thus associated with a specific runout distance $F_{RD}^{-1}(x_s)$. The numerator of Eq. 8 is a measure of the consistency degree between $F_{RD}^{-1}(x_s)$ and $RD_{m,n}$, while the denominator is a normalization factor that considers the consistency degree between $F_{RD}^{-1}(x_s)$ and the runout distance in all the elements of the matrix RD (i.e. all the calibration simulations). ε_{DEM} is incorporated to avoid division by zero in any simulation condition.

3.2.2 Inundation area-based calibration

Finally, because likely eruption scenarios have been also defined using the expected inundation area (e.g. Bevilacqua et al., 2017), we also consider the use of this variable to calibrate the input parameters (in this case as well, no reference inundation polygon is needed to develop the calibration simulations). If we define the cumulative distribution function of inundation area by F_{IA}, we can compute the weight that must be assigned to a calibration simulation characterized by the inundation area $IA_{m,n}$ with the aim of reproducing the predefined probability distribution of inundation area:

$$S_{m,n}^{(5)} := \int_0^1 \frac{\left(\left|IA_{m,n} - F_{IA}^{-1}(x)\right| + \varepsilon_{DEM}^2\right)^{-1}}{\sum_{a=1}^{N}\sum_{b=1}^{N}\left(\left|IA_{a,b} - F_{IA}^{-1}(x)\right| + \varepsilon_{DEM}^2\right)^{-1}} dx \tag{9}$$

where IA is the matrix containing the inundation area of the calibration simulations and the subscripts refer to the indices of this matrix. The reason for including ε_{DEM}^2 is equivalent to that presented previously.

In ECMapProb and BoxMapProb, the number of simulations to be performed in the calibration step is defined by the user. However, in order to mitigate discretization errors, the comparison metrics (i.e. $RMSD$, HD, JI, RD and IA) are interpolated in the input space, giving rise to a sufficiently large matrix, which considers $N = 100$ and preserves the limits of the ranges defined by the user for $H_{0,0}$ and $\tan(\varphi)$. It is worth noting that, as an alternative to the described calibration strategies, our programs also allow the user to define *a priori* the probability distributions adopted to sample the input parameters. Various options are available to set the vent position as well, including pointwise, linear and radial geometries or a set of positions expressly defined by the user, which can be flexibly adopted for testing the influence of collapse position in PDC propagation.

4. Test cases: Results and discussion

Here we present three applications of our calibration strategies. In particular, El Misti volcano (Peru) was adopted to show the use of calibrations based on a reference inundation polygon for constructing probability maps of PDC inundation, through the branching energy cone model. On the other hand, Merapi volcano (Indonesia) was adopted to illustrate the use of calibrations based on the expected distribution of runout distance, while Campi Flegrei (Italy) was selected to show the use of calibrations based on the expected distribution of inundation area. Because most of the PDCs generated at Merapi volcano are derived from dome collapses (i.e. they are frictional flows), we used the branching energy cone model. Instead, since Campi Flegrei eruptions tend to produce dilute, inertial PDCs, they are better described by the box model (Esposti Ongaro et al., 2016). In the latter case, we adopted the traditional formulation instead of the branching one because minor channelization processes are expected in such a flat topography and because this choice allows performing comparisons with the most recent PDC hazard assessments at Campi Flegrei (Neri et al., 2015; Bevilacqua et al., 2017).

5.1 El Misti volcano

El Misti volcano (5,822 m a.s.l.) is located at 13 km NE from Arequipa city (>1 million inhabitants, at an altitude 3,500 m lower than the summit of El Misti). These factors and its potential to develop PDC-forming eruptions (Legros, 2001; Thouret et al., 2001; Harpel et al., 2011; Sandri et al., 2014; Charbonnier et al., 2020) justify the use of this volcano as a case study for illustrating the application of our calibration strategies. In fact, at least three sub-Plinian and Plinian eruptions occurred at El Misti during the last 10,000 years, intercalated with small-magnitude Vulcanian events (Cobeñas et al., 2012). Following Cobeñas et al. (2012) and Charbonnier et al. (2020), we adopted the 2070 cal yr BP Plinian eruption as a reference event to assess PDC hazard at El Misti volcano, which corresponds to a VEI 4 event for which the recurrence rate has been estimated between 2000 and 4000 years (Charbonnier et al., 2020). We stress that the presentation of updated hazard maps is beyond the objectives of this work (for which the reader can consult the official hazard map for El Misti; Mariño et al., 2008). Instead, we aim at presenting an illustrative application of our calibration strategies. For this, we used the inundation polygon of the PDCs derived from the 2070 cal yr BP Plinian eruption (Fig. 3a; Charbonnier et al., 2020) to calibrate the input parameters, considering a fixed collapse position at the summit crater (Fig. 3a), $H_{0,0}$ from 100 m to 2,000 m, and $\tan(\varphi)$ ranging between 0.2 and 1.0.

We performed 400 calibration simulations using the branching energy cone model. Figure 3b-d shows the pseudo-color plots derived from the calibration simulations, based on the following metrics: RMSD, HD and JI. This figure highlights the strong correlation between $H_{0,0}$ and $\tan(\varphi)$ in determining the different similarity indexes and shows that the best-fit conditions of RMSD are quite similar to those of JI, while best-fit conditions of HD tend to show lower values of $\tan(\varphi)$ at equal $H_{0,0}$.

Then, calibration results were used to sample three sets of input parameters, each one derived from the application of a different metric (RMSD, HD and JI, respectively; Fig. 3e-g). With this information, we performed three additional sets of simulations aimed at constructing scenario-based probability maps of PDC inundation. Here we also introduced a small variability in vent position, which was sampled uniformly within a 200 m-radius circle centered in the collapse position used in the calibration simulations (Fig. 3a).

The resulting probability maps of PDC inundation (Fig. 4) are highly consistent between them and with Cobeñas et al. (2012) and Sandri et al. (2014). They show a preferential propagation direction toward NW (i.e., toward the basin and the city of Arequipa, reaching in many cases its suburbs). Runout distance typically ranges between 6 km and 15-17 km (mean value of about 10 km and median value of ~9 km; Fig. 4 and supplementary Table C1). The branching energy cone model predicts non-negligible channelization processes through river Chili, which agrees with the geological record at El Misti volcano, influencing sensibly the inundation probability in the northern portion of Arequipa (Fig. 4). Depending on the adopted calibration procedure, results show probabilities between ~5% and ~10% that a PDC caused by an event similar to the reference eruption will reach the district of Chiguata and probabilities of up to 20% for the NE suburbs of Arequipa (~10-20% for Alto Selva Alegre and ~5-10% for Miraflores; Fig. 4). On the other hand, significant channelization processes toward NE and SE are not apparent in the numerical results. Figure 4 shows that the 50% isolines of the resulting probabilistic maps tend to present a behavior similar to the reference scenario (indicated by a green line in Fig. 4), but it presents shorter propagation distances in the channelization zones. However, the 10% isolines envelope most of the inundation area of the reference scenario also in the channelization domains.

Importantly, channelization through the San Lázaro catchment is significant at proximal and medial zones and small at distal domains, and very weak channelization is modelled along the Huarangal catchment. This is apparently inconsistent with Charbonnier et al. (2020), who recognized these catchments as relevant for the channelization of pyroclastic material to Arequipa. However, we stress that our simulations were calibrated using a specific reference deposit with very limited channelization through these catchments and, more importantly, our collapse positions are located in the summit zone, while the simulations performed by Charbonnier et al. (2020) were developed considering the collapse of already channelized pyroclastic material (in particular, the collapsing material was initially located at the apex of two specific drainage networks, at >2 km from the summit crater). Consequently, as Charbonnier et al. (2020) indicate, their probabilistic maps are not only conditioned on the occurrence of a VEI 4 eruption, but also on the entrance of large volumes of pyroclastic material in two specific drainage networks that threaten Arequipa; while our probabilistic maps are conditioned exclusively on the occurrence of a VEI 4 event. These differences in the objectives and thus in the criteria adopted in the calibration step hinder the development of further comparisons with Charbonnier et al. (2020), and highlight the necessity of considering separately the PDCs initiated from the summit and near the drainage networks at El Misti volcano. In any case, to show that this difference derive from the adoption of different calibration criteria instead of limitations of the branching energy cone model to channelize pyroclastic material, we performed additional simulations with a vent located on the flanks of the volcano, which are displayed in the supplementary Figure C1. These simulations show the potential of the branching energy cone model to predict highly channelized flows along the main drainage networks of El Misti volcano, eventually threatening the city of Arequipa.

4.2 Merapi volcano

Merapi stratovolcano (~2,930 m a.s.l.) is located at ~25 km north of the metropolitan area of Yogyakarta, Central Java, Indonesia. This basaltic-to-basaltic andesitic volcano has presented frequent dome-forming activity during the last centuries. Several of these eruptions have generated PDCs (*"Merapi-type" nuées ardentes*) and subsequent lahars (Boudon et al., 1993; Voight et al., 2000; Voight and Davis, 2000; Bourdier and Abdurachman, 2001; Thouret et al., 2001; Lube et al., 2011; Gertisser et al., 2012; Surono et al., 2012; Charbonnier et al., 2013; Komorowski et al., 2013; Kelfoun et al., 2021). The topography of Merapi, characterized by numerous radial valleys, has exerted a significant effect in the propagation of PDCs, and also the crater configuration and collapse position have influenced the transport direction of recent PDCs (e.g. Charbonnier and Gertisser, 2008). For instance, because of the topographic barriers present at the NE of the volcano summit, most of the recent PDCs propagated towards S, SW and W (Solikhin, 2015).

The frequent occurrence of dome-forming eruptions and the presence of densely populated cities in the surroundings of Merapi justify the use of this volcano as a study case to illustrate the application of our calibration procedures. Moreover, the dynamics of this type of PDCs is dominated by gravitational acceleration on the volcanic slopes and granular frictional dissipation, making them suitable for the use of the branching energy cone model. We remark that the presentation of new hazard maps is beyond the objectives of this article, for which the reader can consult the wide volcanological literature at Merapi (Andreastuti et al., 2000; Itoh et al., 2000; Lavigne et al., 2000; Thouret et al., 2000; Charbonnier and Gertisser, 2012; Mei et al., 2013; Lavigne et al., 2015; Kelfoun et al., 2017) and the official hazard map of this volcano (Sayudi et al., 2010). Instead, we adopt this case study to illustrate the application of calibrations based on the distribution of runout distance.

In fact, the availability of detailed information about the dispersion of PDCs in the past (e.g. Bourdier and Abdurachman, 2001; Solikhin, 2015) allows us to consider the expected distribution of runout distance to calibrate our numerical model. To do this, first we performed 400 calibration simulations using the branching energy cone model and considering a fixed collapse position at the summit crater, $H_{0,0}$ ranging from 40 m to 200 m, and $\tan(\varphi)$ ranging between 0.2 and 1.0. The small range adopted for collapse height is justified by the generation mechanism of most of the PDCs at Merapi, i.e. dome collapse.

Figure 5a-b presents the pseudo-color plots of runout distance and inundation area in the calibration simulations. Because of the high slope that characterizes the volcano flanks in the proximal area (>30º), a significant gap is observed in the simulated runout distances between ~0.2 km (i.e. inside the crater limits) and ~2.5 km (Fig. 5a). In other words, all the simulations that exceeded the crater limits were able to travel at least ~2.5 km from the source due to the high slopes encountered by the PDC in this zone of the volcano.

To define the input probability distribution of runout distance, we adopted the information summarized by Solikhin (2015), who compiled the runout distances of 55 PDCs between 1900 and 2010 (Fig. 5c-d). In particular, the runout distances of these events were fitted considering both gamma and lognormal probability functions (Fig. 5c-d). Although a bimodal distribution could be hypothesized to describe the data, we decided to keep the discussion simpler and focus on the calibration features. The coupling of calibration simulations and the two predefined distributions of runout distance give rise to two sampling probability distributions of input parameters (Figure 5e-f). It is worth noting that the absence of runout distances between ~0.2 km and ~2.5 km in the calibration simulations necessarily translates into the absence of these values of runout distances in the resulting PDC invasion maps. With the two sampling probability distributions of input parameters described previously (Fig. 5e-f), we performed two sets of 500 simulations to construct PDC inundation probability maps. To carry out these simulations, collapse positions were sampled uniformly from a 300 m-radius circle centered in the collapse position used for the calibration simulations (i.e. the volcano summit).

The resulting inundation maps are displayed in Figure 6. Even though we sampled the collapse positions uniformly, results reproduce well the preferential propagation directions observed at Merapi volcano (i.e. S, W, NW and SW), which are also observed in hazard maps derived from the geological record of Merapi volcano (e.g. Figure 4 of Thouret et al., 2000). It is worth noting that the small inundation probabilities simulated at distances of the order of 15 km, which are present in the geological record of Merapi (Newhall et al., 2000), is a consequence of the dataset adopted in the numerical calibration (i.e. PDCs between 1900 and 2010), which implies that our probability maps are conditioned on the occurrence of an eruption that follows the eruption variability of the last century (Solikhin, 2015).

Differences between the results associated with the gamma and lognormal fits are negligible (Fig. 6, Fig. 7a and supplementary Table C2). In these simulations, mean runout distance is 5.8-5.9 km, with 90% confidence intervals of [3.2, 12.1] km and [3.1, 11.5] km for the results associated with gamma and lognormal fits, respectively (supplementary Table C2). The low values of $\mathrm{IA}/(\pi \cdot \mathrm{R}_{\mathrm{max}}^2)$ in numerical simulations, where IA is the inundation area and $\mathrm{R}_{\mathrm{max}}$ is the runout distance, highlights the capacity of the branching energy cone model to reproduce the strong channelization effects related to Merapi's topography (supplementary Table C2). In fact, the branching energy cone model predicts non-negligible channelization processes through different river valleys such as Senowo, Apu, Woro, Opak and Gendol, which agrees with the recent activity at Merapi volcano (Fig. 6). Interestingly, although the last major PDC at Merapi was channelized through the Gendol catchment, our results suggest a dominant channelization effect in Woro and Opak catchments to the south. This apparent inconsistency with the last eruption is instead coherent with the geological record of the last century (Solikhin, 2015).

Figure 7a presents the comparison between the CDFs of the predefined distributions of runout distance, which derive from two fits based on the geological record of Merapi (gamma and lognormal; dashed lines), and the resulting distributions of runout distance in the simulations presented in Figure 6 (continuous lines). The empirical CDF of 55 documented PDCs is also included (Solikhin, 2015). The main contrast between the predefined and resulting CDFs derives from the absence of simulations with runout distances lower than 2.5 km. We speculate that low-runout distance PDCs observed at Merapi can be related to volume-limited block-and-ash flows (or simply a rock-fall rather than a PDC), whose dynamics cannot be modeled by the branching energy cone model. The presence of different families of PDCs at Merapi could be responsible for the bimodal behavior of documented runout distances (Fig. 5c-d). Additional differences between the predefined and resulting CDFs presented in Figure 7a may derive from the use of a calibration based on simulations performed using a single collapse position, while a small uncertainty in collapse position was introduced for the construction of the hazard maps presented in Figure 6.

A major challenge to evaluate the hazard associated with dome collapse at Merapi is the frequent occurrence of changes in the eruption site (Thouret et al., 2000). To demonstrate the model capability to simulate the effect associated with collapse position, we performed four additional sets of simulations considering collapse positions in different zones of the volcano. In particular, collapse positions were sampled uniformly within different regions of a 300 m-radius circle centered in the volcano summit. Four regions were considered: NW, NE, SW and SE. On the other hand, $H_{0,0}$ and $\tan(\varphi)$ were sampled considering the gamma fit used previously (Fig. 5e). Results are presented in Figure 8, indicating that small differences in the collapse position (e.g. of the order of hundreds of meters) are able to change dramatically the expected propagation of PDCs and the valleys involved. In particular, PDCs derived from collapsing domes located in the NW flank of Merapi volcano tends to be channelized through the valleys Apu and Senowo, and a significant part of these PDCs is propagated toward SW (Fig. 8a). Importantly, volcano topography at the NE flank tends to redirect PDCs mainly through the valleys Apu (i.e. NW) and Woro (i.e. SSE; Fig. 8b). This is consistent with the geological record of Merapi. On the other hand, PDCs produced from collapsing domes situated in the SW flank tend to be channelized through the valleys Senowo, Putih, Bebeng, Krasak, Boyong, Opak and Gendol (Fig. 8c). Finally, collapses at the SE flank of Merapi tend to be channelized through the valleys Opak, Gendol and Woro. Figure 7b shows the empirical CDFs of the runout distances modelled in the simulations presented in Fig. 8, with only minor differences between the different sets of simulations.

We remark that these maps are conditioned on the occurrence of a PDC derived from the collapse of a summit dome, which is not the only mechanism able to produce PDCs at Merapi. In fact, this volcano has presented large explosive eruptions in historic times, such as the 1872 eruption (Hartmann, 1934). Another limitation is related to the absence of numerical simulations able to produce runout distances lower than 2.5 km. Despite this, our results highlight the model capability to capture the strong control exerted by collapse position in the propagation of PDCs. A more extensive analysis of the dependence between the location of collapsing domes and transport of the resulting PDCs may provide key information for the design and implementation of effective, focalized measures for volcanic hazard mitigation.

4.3 Campi Flegrei

Campi Flegrei, located on the Campanian plain in Southern Italy, is a 12 km wide caldera that includes a highly urbanized area and a significant portion of the city of Naples. The volcanic activity of Campi Flegrei during the last 15 kyr has been separated in three epochs of temporally clustered eruptions, which include at least 70 explosive events (e.g. Di Vito et al., 1999; Smith et al., 2011; Bevilacqua et al., 2016; Isaia et al., 2019). Among the products of these eruptions, PDCs represent the main volcanic hazard at Campi Flegrei (Lirer et al., 2001; Alberico et al., 2002; Orsi et al., 2004; Rossano et al., 2004; Todesco et al., 2006; Orsi et al., 2009; Alberico et al., 2011; Neri et al., 2015; Tierz et al., 2016b; Bevilacqua et al., 2017) but their assessment is made more challenging by the large uncertainty in the position of future vents (Alberico et al., 2002; Orsi et al., 2004; Selva et al., 2012; Bevilacqua et al., 2015; Bevilacqua et al., 2017; Rivalta et al., 2019; Bevilacqua et al., 2020). We adopted this case study to show the application of a calibration based on the distribution of inundation area.

In fact, the availability of detailed information about the dispersion of PDCs in the past allows considering the expected distribution of inundation area to calibrate the box model. To do this, we performed two sets of 900 calibration simulations each? by adopting the traditional formulation of the box model, with the collapsing volume ranging from 10^6 to 10^{11} m^3 and the initial concentration of solid particles between 0.5 vol. % and 4.0 vol. %. The other input parameters of the box model were fixed (sedimentation velocity of 0.6 m/s, Froude number of 1.1, pyroclasts density of 1500 kg/m^3 and ambient gas density of 1.1 kg/m^3). These two sets of simulations differ in their collapse positions, which were set at Monte Nuovo and Agnano, respectively (Fig. 9a), and allow to calculate the inundation area as a function of the two variable input parameters (Fig. 9b-c). It is worth noting that, although the uncertainty in vent position in this volcanic field may hinder the use of a fixed vent position for calibration purposes, the absence of major topographic barriers at Campi Flegrei (with the exception of the caldera rim of ~160 m height and the boundary of the Agnano plain of ~110 m height) produces only small differences in the calibration results as a function of the collapse position. In particular, we adopted the calibration data of Monte Nuovo and Agnano as representative of the western and eastern sectors of Campi Flegrei, respectively. In the following we further evaluate the validity of this assumption.

Because the calibration procedure described in Section 3.2.2 needs the input of a probability distribution of inundation area, we used the information summarized by Neri et al. (2015), which relies largely on Orsi et al. (2004). In particular, we followed the strategy of Neri et al. (2015) and Bevilacqua et al. (2017) to consider the variability of inundation area in 47 documented PDCs, the effect of eventual underestimations of the area of PDC deposits, and the presence of "lost" deposits in the dataset, considering the western and eastern domains of Campi Flegrei separately because significant differences have been recognized in the typical scale of their eruptions (for additional details, see Bevilacqua et al., 2017). This allowed us to define the expected distribution of inundation area in the two regions of Campi Flegrei, which are displayed as cumulative curves in Figure 9d-e. These results show that the inundation area of PDCs generated at the eastern sector of Campi Flegrei tends to be significantly larger than that expected in the western portion of this volcanic field.

The coupling of the calibration simulations (Fig. 9b-c) and the expected distributions of inundation area (Fig. 9d-e) gives rise to two sampling probability distributions of input parameters, which are displayed in Figure 10. These results show a strong correlation between the two input parameters in the calculation the sampling probability of the model inputs, suggesting that interdependent sampling strategies of the model inputs should be preferred (Fig. 10). As expected, the peak of sampling probability for the western sector of Campi Flegrei (computed for collapsing volumes of $V_0 = 10^7 - 3 \cdot 10^8$ m^3 and volumes of pyroclasts of $V_0\phi = 4 \cdot 10^5 - 1.6 \cdot 10^6$ m^3) is associated with much smaller PDCs than that predicted for the eastern zone of this caldera (computed for collapsing volumes of $V_0 = 3 \cdot 10^8 - 2 \cdot 10^9$ m^3 and volumes of pyroclasts of $V_0\phi = 8 \cdot 10^6 - 1.2 \cdot 10^7$ m^3), with differences of one order of magnitude (Fig. 10).

With this information, we performed two sets of 3,000 simulations to construct PDC inundation probability maps for the two sectors of Campi Flegrei. To carry out these simulations, collapse positions were sampled using the vent opening probability map presented by Bevilacqua et al. (2015). Note that this map includes uncertainty ranges but, for simplicity, in this work we adopted the mean value map. We also resampled all the vents located offshore and considered separately the western and eastern sectors of Campi Flegrei, using the limits adopted by Bevilacqua et al. (2017). On the other hand, the sea surface has been considered as a flat topography with no consideration of water influence in the PDC propagation dynamics.

Numerical results, visualized in a GIS environment, are displayed in Figure 11a-b. We remark that these maps are conditioned on the occurrence of a PDC-forming eruption in the western and eastern sectors of Campi Flegrei, respectively, without assumptions associated with its magnitude or intensity, in contrast to the maps obtained for El Misti volcano. We also include the combined probabilistic map of PDC inundation (Fig. 11c), defined using the relative weights of the two sectors of Campi Flegrei in the vent opening maps of Bevilacqua et al. (2015), i.e. 30.7%

for the western sector and 69.3% for the eastern sector. For an eruption located in the western sector of Campi Flegrei, our simulations show a peak of PDC inundation probability of about 30% at Averno, being strongly consistent with Bevilacqua et al. (2017). Instead, for an eruption located in the eastern portion of this volcanic system, numerical results show a maximum PDC inundation probability of ~60% at Astroni and Agnano, with probabilities around 15-20% of having a PDC able to overcome the Posillipo Hill, again in agreement with the results presented by Bevilacqua et al. (2017). Note that the differences in the maximum values of PDC inundation probability between the two sectors of Campi Flegrei are mainly derived from the scale of the PDCs expected, which are much larger in the eastern sector. The combined probability map of PDC inundation, which is not conditioned on the sector of the source position, presents a maximum value of ~43% at Agnano and Astroni, and a probability of ~10-15% of overcoming the Posillipo Hill. The consistency between our results and Bevilacqua et al. (2017) can be considered an expected result because we used the same geological dataset to calibrate the models. However, it is worth stressing that the calibration procedures are completely different, showing that a calibration based on a single source point can be enough in volcanic contexts characterized by small scale topographic barriers as Campi Flegrei.

Finally, Figure 12 presents the comparison between the CDFs of the predefined distributions of inundation area (continuous red lines) and the resulting distributions of this variable in the simulations of the probability maps presented in Figure 11a-b (dashed blue lines). The empirical CDF of inundation area in the geological record of Campi Flegrei is also displayed (black line). The strong agreement between the prescribed and the resulting distributions of inundation area further confirms that a calibration procedure based on simulations performed using a single source point is able to capture well the dependence between the box model input parameters and the resulting inundation area in this volcanic system, where the topographic roughness is small.

5. Summary and conclusions

Although numerical models have become a fundamental aspect in the assessment of volcanic hazard and in the design of volcanic risk mitigation strategies (e.g. Ferrés et al., 2013; Sandri et al., 2014; Bevilacqua et al., 2017; Charbonnier et al., 2020; Clarke et al., 2020; Esposti Ongaro et al., 2020b), the large variety of criteria used to calibrate their input parameters often limits the development of comparisons between different numerical models, which is a critical step for their validation (Esposti Ongaro et al., 2020a). In this work we propose a set of structured and reproducible procedures to calibrate the input parameters of numerical models, which are based on the characteristics of past PDCs in the studied volcanic system. This information can be described in terms of:

(a) A reference inundation polygon derived from a specific eruption. Three parameters to compute the similarity index between this polygon and a set of calibration simulations have been considered (RMSD, Hausdorff distance, and Jaccard Index). These results can be used to define different sampling probability distributions of the input parameters, which in turn can be adopted to extract a set of calibrated inputs to use in numerical simulations. The application of these calibrations enables the construction of probabilistic maps of PDC inundation conditioned on the occurrence of an event similar to the reference scenario (i.e. scenario-based hazard assessment, see Section 4.1).

(b) The distribution of runout distance or inundation area of past PDCs. This information, along with the results of the calibration simulations, allows sampling a set of input parameters able to reflect the eruptive history of the volcano. These two procedures, whose application involves a large knowledge of the characteristics of the studied volcanic system, are able to produce PDC inundation probabilistic maps conditioned on the occurrence of a PDC-forming eruption without assumptions associated with its characteristics (e.g. magnitude or intensity, see Sections 4.2 and 4.3).

The suitability of the different calibration procedures will be naturally controlled by the availability of detailed information of the studied volcanic system and by the approach used to assess the hazard derived from PDCs (e.g. based on a specific scenario or not). All these strategies allow considering the interaction of the input parameters in controlling the numerical results (in other words, input parameters are not sampled independently). In fact, all the tested cases exhibit a strong interdependence between the input parameters in the resulting functions of sampling probability, suggesting that calibration strategies that consider interdependent sampling should be preferred for the construction of probabilistic maps of PDC inundation. Thereby, through the use of these calibration strategies, we reduce the biases derived from arbitrary user choices/assumptions in the construction of PDC hazard maps, which have been often necessary due to lack of ad-hoc data.

We have illustrated our calibration strategies by applying them to three volcanoes: El Misti, Merapi and Campi Flegrei. In particular, the El Misti example illustrates the use of calibrations based on a reference inundation polygon related to a specific eruption; the Merapi example shows the use of a calibration based on the expected distribution of runout distance, and the analysis of Campi Flegrei was developed by using a calibration based on the expected distribution of inundation area. In general terms, results are strongly consistent with previous hazard assessments and with the geological record of these volcanic systems (e.g., Cobeñas et al., 2012; Sandri et al., 2014; Neri et al., 2015; Solikhin, 2015; Bevilacqua et al., 2017). In any case, we stress that our results are not intended to represent updated hazard maps of these well-documented volcanoes, for which the reader can consult the official maps and other recent studies of volcanic hazard (e.g. Mariño et al., 2008; Sayudi et al., 2010; Sandri et al., 2014; Neri et al., 2015; Bevilacqua et al., 2017; Charbonnier et al., 2020).

The different calibration procedures described here were implemented on improved, user-friendly versions of the programs ECMapProb and BoxMapProb, whose functionalities and user manuals are presented for the first time in this article. These open-source and freely downloadable programs adopt the traditional and branching formulations of the energy cone and the box models (Aravena et al., 2020), respectively, and thus they present different applicability fields (frictional and inertial flows, respectively). In addition to the presented calibration procedures, we stress that ECMapProb and BoxMapProb allow the user to define *a priori* different probability distributions to sample the model inputs. Different modalities are also available to set vent position, which can be adopted for coupling kinetic models with vent opening probability maps (Bevilacqua el al., 2021), as shown in Section 4.3. We also note that the traditional and branching formulations of kinetic models do not involve large computational requirements and allow constructing PDC inundation maps on simple CPU computers. All these characteristics make our programs useful tools for the early assessment of PDC volcanic hazards, allowing for the construction of probabilistic inundation maps considering reproducible calibration procedures, able to reduce the biases introduced by user choices.

Code availability

ECMapProb is available in https://github.com/AlvaroAravena/ECMapProb (Apache 2.0 license). BoxMapProb is available in https://github.com/AlvaroAravena/BoxMapProb (Apache 2.0 license).

Acknowledgement

We appreciate the systematic compilation of volcanological data presented by Dr. A. Solikhin in his doctoral thesis, which was strongly useful for one of the applications presented here. Alvaro Aravena was financed by the French government IDEX-ISITE initiative 16-IDEX-0001 (CAP 20-25).

References

Alberico, I., Lirer, L., Petrosino, P., and Scandone, R. (2002). A methodology for the evaluation of long-term volcanic risk from pyroclastic flows in Campi Flegrei (Italy). Journal of Volcanology and Geothermal Research, 116(1-2), 63-78. https://doi.org/10.1016/S0377-0273(02)00211-1

Alberico, I., Petrosino, P., and Lirer, L. (2011). Volcanic hazard and risk assessment in a multi-source volcanic area: the example of Napoli city (Southern Italy). *Natural Hazards and Earth System Sciences,* 11(4), 1057-1070. https://doi.org/10.5194/nhess-11-1057-2011

Andreastuti, S., Alloway, B., and Smith, I. (2000). A detailed tephrostratigraphic framework at Merapi Volcano, Central Java, Indonesia: implications for eruption predictions and hazard assessment. *Journal of Volcanology and Geothermal Research*, 100(1-4), 51-67. https://doi.org/10.1016/S0377-0273(00)00133-5

Aravena, A., Cioni, R., Bevilacqua, A., de' Michieli Vitturi, M., Esposti Ongaro, T., and Neri, A. (2020). Tree-branching-based enhancement of kinetic energy models for reproducing channelization processes of pyroclastic density currents. *Journal of Geophysical Research: Solid Earth*, 125(7), e2019JB019271. https://doi.org/10.1029/2019JB019271

Asmussen, S., and Hering, H. (1983). Branching processes. Springer.

Bevilacqua, A. (2016). Doubly stochastic models for volcanic hazard assessment at Campi Flegrei caldera. Springer.

Bevilacqua, A., Aravena, A., Neri, A., Gutiérrez, E., Escobar, D., Schliz, M., Aiuppa, A., and Cioni, R. (2021). Thematic vent opening probability maps and hazard assessment of small-scale pyroclastic density currents in the San Salvador volcanic complex (El Salvador) and Nejapa-Chiltepe volcanic complex (Nicaragua). *Natural Hazards and Earth System Sciences*, 21, 1639–1665. https://doi.org/10.5194/nhess-21-1639-2021

Bevilacqua, A., Isaia, R., Neri, A., Vitale, S., Aspinall, W., Bisson, M., Flandoli, F., Baxter, P., Bertagnini, A., and Esposti Ongaro, T. (2015). Quantifying volcanic hazard at Campi Flegrei caldera (Italy) with uncertainty assessment: 1. Vent opening maps. *Journal of Geophysical Research: Solid Earth*, 120(4), 2309-2329. https://doi.org/10.1002/2014JB011775

Bevilacqua, A., Neri, A., Bisson, M., Esposti Ongaro, T., Flandoli, F., Isaia, R., Rosi, M., and Vitale, S. (2017). The effects of vent location, event scale, and time forecasts on pyroclastic density current hazard maps at Campi Flegrei caldera (Italy). *Frontiers in Earth Science*, 5, 72. https://doi.org/10.3389/feart.2017.00072

Bevilacqua, A., Neri, A., De Martino, P., Isaia, R., Novellino, A., Tramparulo, F., and Vitale, S. (2020). Radial interpolation of GPS and leveling data of ground deformation in a resurgent caldera: application to Campi Flegrei (Italy). *Journal of Geodesy*, 94(2), 1-27. https://doi.org/10.1007/s00190-020-01355-x

Bevilacqua, A., Patra, A., Bursik, M., Pitman, E., Macías, J., Saucedo, R., and Hyman, D. (2019). Probabilistic forecasting of plausible debris flows from Nevado de Colima (Mexico) using data from the Atenquique debris flow, 1955. *Natural Hazard and Earth System Sciences*, 19, 791–820. https://doi.org/10.5194/nhess-19-791-2019

Biass, S., Bonadonna, C., Connor, L., and Connor, C. (2016). TephraProb: a Matlab package for probabilistic hazard assessments of tephra fallout. *Journal of Applied Volcanology*, 5, 10. https://doi.org/10.1186/s13617-016-0050-5

Boudon, G., Camus, G., Gourgaud, A., and Lajoie, J. (1993). The 1984 nuée-ardente deposits of Merapi volcano, Central Java, Indonesia: stratigraphy, textural characteristics, and transport mechanisms. *Bulletin of Volcanology*, 55(5), 327-342. https://doi.org/10.1007/BF00301144

Bourdier, J.-L., and Abdurachman, E. (2001). Decoupling of small-volume pyroclastic flows and related hazards at Merapi volcano, Indonesia. *Bulletin of Volcanology*, 63, 309-325. https://doi.org/10.1007/s004450100133

Campbell, C. (2006). Granular material flows–an overview. *Powder Technology*, 162(3), 208-229. https://doi.org/10.1016/j.powtec.2005.12.008

Charbonnier, S., Germa, A., Connor, C., Gertisser, R., Preece, K., Komorowski, J., Lavigne, F., Dixon, T., and Connor, L. (2013). Evaluation of the impact of the 2010 pyroclastic density currents at Merapi volcano from high-resolution satellite imagery, field investigations and numerical simulations. *Journal of Volcanology and Geothermal Research*, 261, 295-315.

Charbonnier, S., and Gertisser, R. (2008). Field observations and surface characteristics of pristine block-and-ash flow deposits from the 2006 eruption of Merapi Volcano, Java, Indonesia. *Journal of Volcanology and Geothermal Research*, 177(4), 971-982.

Charbonnier, S., and Gertisser, R. (2012). Evaluation of geophysical mass flow models using the 2006 block-and-ash flows of Merapi Volcano, Java, Indonesia: Towards a short-term hazard assessment tool. *Journal of Volcanology and Geothermal Research*, 231, 87-108.

Charbonnier, S., Thouret, J., Gueugneau, V., and Constantinescu, R. (2020). New insights into the 2070 cal yr BP pyroclastic currents at El Misti volcano (Peru) from field investigations, satellite imagery and probabilistic modeling. *Frontiers in Earth Science*, 8, 398.

Cioni, R., Tadini, A., Gurioli, L., Bertagnini, A., Mulas, M., Bevilacqua, A., and Neri, A. (2020). Estimating eruptive parameters and related uncertainties for pyroclastic density currents deposits: worked examples from Somma-Vesuvius (Italy). *Bulletin of Volcanology*, 82(9), 1-20.

Clarke, B., Tierz, P., Calder, E., and Yirgu, G. (2020). Probabilistic volcanic hazard assessment for pyroclastic density currents from pumice cone eruptions at Aluto volcano, Ethiopia. *Frontiers in Earth Science*, 8, 348.

Cobeñas, G., Thouret, J., Bonadonna, C., and Boivin, P. (2012). The c. 2030 yr BP Plinian eruption of El Misti volcano, Peru: eruption dynamics and hazard implications. *Journal of Volcanology and Geothermal Research*, 241, 105-120.

de' Michieli Vitturi, M., Esposti Ongaro, T., Lari, G., and Aravena, A. (2019). IMEX_SfloW2D 1.0: a depth-averaged numerical flow model for pyroclastic avalanches. *Geoscientific Model Development*, 12.

de' Michieli Vitturi, M., and Tarquini, S. (2018). MrLavaLoba: A new probabilistic model for the simulation of lava flows as a settling process. *Journal of Volcanology and Geothermal Research*, 349, 323-334.

Di Vito, M. A., Isaia, R., Orsi, G., Southon, J., De Vita, S., D'Antonio, M., Pappalardo, L., and Piochi, M. (1999). Volcanism and deformation since 12,000 years at the Campi Flegrei caldera (Italy). *Journal of Volcanology and Geothermal Research*, 91(2-4), 221-246. https://doi.org/10.1016/S0377-0273(99)00037-2

Doyle, E., Hogg, A., Mader, H., and Sparks, R. (2010). A two-layer model for the evolution and propagation of dense and dilute regions of pyroclastic currents. *Journal of Volcanology and Geothermal Research*, 190(3-4), 365-378.

Druitt, T. (1998). Pyroclastic density currents. Geological Society, London, Special Publications, 145(1), 145-182.

Dufek, J., Esposti Ongaro, T., and Roche, O. (2015). Pyroclastic density currents: processes and models, The Encyclopedia of Volcanoes.

Esposti Ongaro, T., Cerminara, M., Charbonnier, S., Lube, G., and Valentine, G. (2020a). A framework for validation and benchmarking of pyroclastic current models. *Bulletin of Volcanology*, 82(6).

Esposti Ongaro, T., Komorowski, J.C., Legendre, Y., and Neri, A. (2020b). Modelling pyroclastic density currents from a subplinian eruption at La Soufrière de Guadeloupe (West Indies, France). *Bulletin of Volcanology*, 82(12), 1-26.

Esposti Ongaro, T., Orsucci, S., and Cornolti, F. (2016). A fast, calibrated model for pyroclastic density currents kinematics and hazard. *Journal of Volcanology and Geothermal Research*, 327, 257-272.

Esposti Ongaro, T., Widiwijayanti, C., Clarke, A., Voight, B., and Neri, A. (2011). Multiphase-flow numerical modeling of the 18 May 1980 lateral blast at Mount St. Helens, USA. *Geology*, 39(6), 535-538.

Ferrés, D., Delgado-Granados, H., Gutiérrez, R., Farraz, I., Hernández, E., Pullinger, C., and Escobar, C. (2013). Explosive volcanic history and hazard zonation maps of Boquerón Volcano (San Salvador volcanic complex, El Salvador). *Geological Society of America Special Papers*, 4(498), 201-230.

Gertisser, R., Charbonnier, S., Keller, J., and Quidelleur, X. (2012). The geological evolution of Merapi volcano, Central Java, Indonesia. *Bulletin of Volcanology*, 74(5), 1213-1233.

Haccou, P., Jagers, P., and Vatutin, V. (2005). Branching processes: variation, growth, and extinction of populations. Cambridge University Press.

Harpel, C. J., de Silva, S., and Salas, G. (2011). The 2 ka eruption of Misti volcano, Southern Peru—the most recent Plinian eruption of Arequipa's iconic volcano (Vol. 484). *Geological Society of America*.

Harris, T. (1963). The theory of branching processes. Springer-Verlag Berlin Heidelberg.

Hartmann, M. (1934). Der grosse Ausbruch des Vukanes G. Merapi (Mittel Java) im Jahre 1872. *Vulkanologische und Seismologische Mededeelingen*, 13.

Hayashi, J., and Self, S. (1992). A comparison of pyroclastic flow and debris avalanche mobility. *Journal of Geophysical Research: Solid Earth*, 97(B6), 9063-9071.

Hsu, K. (1975). Catastrophic debris streams (sturzstroms) generated by rockfalls. *Geological Society of America Bulletin*, 86(1), 129-140.

Huppert, H.E., and Simpson, J.E. (1980). The slumping of gravity currents. *Journal of Fluid Mechanics*, 99(4), 785-799.

Hyman, D., Bevilacqua, A., and Bursik, M. (2019). Statistical theory of probabilistic hazard maps: a probability distribution for the hazard boundary location. *Natural Hazard and Earth System Sciences*, 19(7), 1347-1363. https://doi.org/10.5194/nhess-19-1347-2019

Isaia, R., Vitale, S., Marturano, A., Aiello, G., Barra, D., Ciarcia, S., Iannuzzi, E., & Tramparulo, F. (2019). High-resolution geological investigations to reconstruct the long-term ground movements in the last 15 kyr at Campi Flegrei caldera (southern Italy). *Journal of Volcanology and Geothermal Research*, 385, 143-158. https://doi.org/10.1016/j.jvolgeores.2019.07.012

Itoh, H., Takahama, J., Takahashi, M., and Miyamoto, K. (2000). Hazard estimation of the possible pyroclastic flow disasters using numerical simulation related to the 1994 activity at Merapi Volcano. *Journal of Volcanology and Geothermal Research*, 100(1-4), 503-516.

Kelfoun, K. (2011). Suitability of simple rheological laws for the numerical simulation of dense pyroclastic flows and long-runout volcanic avalanches. *Journal of Geophysical Research: Solid Earth*, 116(B8).

Kelfoun, K., Gueugneau, V., Komorowski, J., Aisyah, N., Cholik, N., and Merciecca, C. (2017). Simulation of block-and-ash flows and ash-cloud surges of the 2010 eruption of Merapi volcano with a two-layer model. *Journal of Geophysical Research: Solid Earth*, 122(6), 4277-4292.

Kelfoun, K., Samaniego, P., Palacios, P., and Barba, D. (2009). Testing the suitability of frictional behaviour for pyroclastic flow simulation by comparison with a well-constrained eruption at Tungurahua volcano (Ecuador). *Bulletin of Volcanology*, 71(9), 1057.

Kelfoun, K., Santoso, A.B., Latchimy, T., Bontemps, M., Nurdien, I., Beauducel, F., Fahmi, A., Putra, R., Dahamna, N., Laurin, A., Rizal, M.H., Sukmana, J.T., and Gueugneau, V. (2021). Growth and collapse of the 2018–2019 lava dome of Merapi volcano. *Bulletin of Volcanology*, 83(2), 1-13.

Komorowski, J., Jenkins, S., Baxter, P., Picquout, A., Lavigne, F., Charbonnier, S., Gertisser, R., Preece, K., Cholik, N., and Budi-Santoso, A. (2013). Paroxysmal dome explosion during the Merapi 2010 eruption: processes and facies relationships of associated high-energy pyroclastic density currents. *Journal of Volcanology and Geothermal Research*, 261, 260-294.

Lavigne, F., Morin, J., and Surono, M. (2015). Atlas of Merapi Volcano. Laboratoire de Géographie Physique, Meudon, France.

Lavigne, F., Thouret, J., Voight, B., Suwa, H., and Sumaryono, A. (2000). Lahars at Merapi volcano, Central Java: an overview. *Journal of Volcanology and Geothermal Research*, 100(1-4), 423-456.

Legros, F. (2001). Tephra stratigraphy of Misti volcano, Peru. *Journal of South American Earth Sciences*, 14(1), 15-29.

Lirer, L., Petrosino, P. and Alberico, I. (2001). Hazard assessment at volcanic fields: the Campi Flegrei case history. *Journal of Volcanology and Geothermal Research*, 112(1-4): 53-73.

Lube, G., Breard, E., Esposti Ongaro, T., Dufek, J., and Brand, B. (2020). Multiphase flow behaviour and hazard prediction of pyroclastic density currents. *Nature Reviews Earth & Environment*, 1-18.

Lube, G., Cronin, S., and Thouret, J. (2011). Kinematic characteristics of pyroclastic density currents at Merapi and controls on their avulsion from natural and engineered channels. *GSA Bulletin*, 123(5-6), 1127-1140.

Macías, J., Capra, L., Arce, J., Espíndola, J., García-Palomo, A., and Sheridan, M. (2008). Hazard map of El Chichón volcano, Chiapas, México: Constraints posed by eruptive history and computer simulations. *Journal of Volcanology and Geothermal Research*, 175(4), 444-458.

Malin, M., and Sheridan, M. (1982). Computer-assisted mapping of pyroclastic surges. *Science*, 217(4560), 637-640.

Mariño, J., Rivera, M., Cacya, L., Thouret, J.-C., Macedo, L., Salas, G., Siebe, C., Tilling, R., Sheridan, M., Chávez, A., and Zuñiga, S. (2008). Mapa de Peligros del Volcán Misti. Instituto Geológico Minero y Metalúrgico (INGEMMET), Direccion de Geologia Ambiental y Riesgo.

Mei, E., Lavigne, F., Picquout, A., De Bélizal, E., Brunstein, D., Grancher, D., Sartohadi, J., Cholik, N., and Vidal, C. (2013). Lessons learned from the 2010 evacuations at Merapi volcano. *Journal of Volcanology and Geothermal Research*, 261, 348-365.

Neri, A., Bevilacqua, A., Esposti Ongaro, T., Isaia, R., Aspinall, W., Bisson, M., Flandoli, F., Baxter, P., Bertagnini, A., and Iannuzzi, E. (2015). Quantifying volcanic hazard at Campi Flegrei caldera (Italy) with uncertainty assessment: 2. Pyroclastic density current invasion maps. *J. Geophys. Res.*, 120(4), 2330-2349.

Neri, A., Esposti Ongaro, T., Macedonio, G., and Gidaspow, D. (2003). Multiparticle simulation of collapsing volcanic columns and pyroclastic flow. *J. Geophys. Res.*, 108(B4).

Newhall, C. G., Bronto, S., Alloway, B., Banks, N. G., Bahar, I., Del Marmol, M. A., ... and Wirakusumah, A. D. (2000). 10,000 Years of explosive eruptions of Merapi Volcano, Central Java: archaeological and modern implications. *Journal of Volcanology and Geothermal Research*, 100(1-4), 9-50. https://doi.org/10.1016/S0377-0273(00)00132-3

Ogburn, S., Berger, J., Calder, E., Lopes, D., Patra, A., Pitman, E., Rutarindwa, R., Spiller, E., and Wolpert, R. (2016). Pooling strength amongst limited datasets using hierarchical Bayesian analysis, with application to pyroclastic density current mobility metrics. *Statistics in Volcanology,* 2, 1-26. https://doi.org/10.5038/2163-338X.2.1

Ogburn, S., and Calder, E. (2017). The relative effectiveness of empirical and physical models for simulating the dense undercurrent of pyroclastic flows under different emplacement conditions. *Frontiers in Earth Science*, 5, 83.

Orsi, G., Di Vito, M. and Isaia, R. (2004). Volcanic hazard assessment at the restless Campi Flegrei caldera. *Bulletin of Volcanology*, 66(6): 514-530.

Orsi, G., Di Vito, M., Selva, J. and Marzocchi, W. (2009). Long-term forecast of eruption style and size at Campi Flegrei caldera (Italy). *Earth and Planetary Science Letters*, 287(1-2): 265-276.

Patra, A., Bauer, A., Nichita, C., Pitman, E., Sheridan, M., Bursik, M., Rupp, B., Webber, A., Stinton, A., and Namikawa, L. (2005). Parallel adaptive numerical simulation of dry avalanches over natural terrain. *Journal of Volcanology and Geothermal Research*, 139(1-2), 1-21.

Patra, A., Bevilacqua, A., Akhavan-Safaei, A., Pitman, E., Bursik, M., and Hyman, D. (2020). Comparative analysis of the structures and outcomes of geophysical flow models and modeling assumptions using uncertainty quantification. *Frontiers in Earth Science*, 8, 275. https://doi.org/10.3389/feart.2020.00275

Pudasaini, S. P., and Domnik, B. (2009). Energy considerations in accelerating rapid shear granular flows. *Nonlinear Processes in Geophysics*, 16(3), 399-407. https://doi.org/10.5194/npg-16-399-2009

Rivalta, E., Corbi, F., Passarelli, L., Acocella, V., Davis, T. and Di Vito, M., (2019). Stress inversions to forecast magma pathways and eruptive vent location. *Science Advances*, 5(7).

Roche, O., Phillips, J., and Kelfoun, K. (2013). Pyroclastic density currents, Modeling Volcanic Processes: The Physics and Mathematics of Volcanism.

Rossano, S., Mastrolorenzo, G. and De Natale, G. (2004). Numerical simulation of pyroclastic density currents on Campi Flegrei topography: a tool for statistical hazard estimation. *Journal of Volcanology and Geothermal Research*, 132(1): 1-14.

Rutarindwa, R., Spiller, E., Bevilacqua, A., Bursik, M., and Patra, A. (2019). Dynamic probabilistic hazard mapping in the Long Valley Volcanic Region CA: integrating vent opening maps and statistical surrogates of physical models of pyroclastic density currents. *Journal of Geophysical Research: Solid Earth*, 124(9), 9600-9621.

Sandri, L., Thouret, J., Constantinescu, R., Biass, S., and Tonini, R. (2014). Long-term multi-hazard assessment for El Misti volcano (Peru). *Bulletin of Volcanology*, 76(2), 771.

Sandri, L., Tierz, P., Costa, A., and Marzocchi, W. (2018). Probabilistic hazard from pyroclastic density currents in the Neapolitan area (Southern Italy). *Journal of Geophysical Research: Solid Earth*, 123(5), 3474-3500.

Sayudi, D.S., Nurnaning A., Juliani Dj., and Muzani, M. (2010). Peta Kawasan Rawan Bencana Gunungapi Merapi, Jawa Tengah Dan Daerah Istimewa Yogyakarta 2010. Center for Volcanology and Geological Hazard Mitigation.

Scollo, S., Tarantola, S., Bonadonna, C., Coltelli, M., and Saltelli, A. (2008). Sensitivity analysis and uncertainty estimation for tephra dispersal models. *Journal of Geophysical Research: Solid Earth*, 113(B6).

Selva, J., Orsi, G., Di Vito, M., Marzocchi, W. and Sandri, L., 2012. Probability hazard map for future vent opening at the Campi Flegrei caldera, Italy. *Bulletin of Volcanology*, 74(2): 497-510.

Sheridan, M., Hubbard, B., Carrasco-Núñez, G., and Siebe, C. (2004). Pyroclastic flow hazard at Volcán Citlaltépetl. *Natural Hazards*, 33(2), 209-221.

Sheridan, M., and Macías, J. (1995). Estimation of risk probability for gravity-driven pyroclastic flows at Volcan Colima, Mexico. *Journal of Volcanology and Geothermal Research*, 66(1-4), 251-256.

Sheridan, M., and Malin, M. (1983). Application of computer-assisted mapping to volcanic hazard evaluation of surge eruptions: Vulcano, Lipari, and Vesuvius. *Journal of Volcanology and Geothermal Research*, 17(1-4), 187-202.

Smith, V., Isaia, R. and Pearce, N. (2011). Tephrostratigraphy and glass compositions of post-15 kyr Campi Flegrei eruptions: implications for eruption history and chronostratigraphic markers. *Quaternary Science Reviews*, 30(25-26): 3638-3660.

Solikhin, A. (2015). Geology, tectonics and post-2001 eruptive activity interpreted from high-spatial resolution satellite imagery: the case study of Merapi and Seremu volcanoes, Indonesia. PhD. Thesis, Earth Sciences. Université Blaise Pascal - Clermont-Ferrand II.

Spiller, E., Bayarri, M., Berger, J., Calder, E., Patra, A., Pitman, E., and Wolpert, R. (2014). Automating emulator construction for geophysical hazard maps. *SIAM/ASA Journal on Uncertainty Quantification*, 2(1), 126-152.

Surono, Jousset, P., Pallister, J., Boichu, M., Buongiorno, M., Budisantoso, A., Costa, F., Andreastuti, S., Prata, F., Schneider, D., Clarisse, L., Humaida, H., Sumarti, S., Bignami, C., Griswold, J., Carn, S., Oppenheimer, C., and Lavigne, F. (2012). The 2010 explosive eruption of Java's Merapi volcano–a '100-year'event. *Journal of Volcanology and Geothermal Research*, 241-242, 121-135.

Tadini, A., Bevilacqua, A., Neri, A., Cioni, R., Biagioli, G., de' Michieli Vitturi, M., and Esposti Ongaro, T. (2021). Reproducing pyroclastic density current deposits of the 79 CE eruption of the Somma–Vesuvius volcano using the box-model approach. *Solid Earth*, 12(1), 119-139.

Thouret, J.-C., Lavigne, F., Kelfoun, K., and Bronto, S. (2000). Toward a revised hazard assessment at Merapi volcano, Central Java. *Journal of Volcanology and Geothermal Research*, 100(1-4), 479-502.

Thouret, J., Finizola, A., Fornari, M., Legeley-Padovani, A., Suni, J., and Frechen, M. (2001). Geology of El Misti volcano near the city of Arequipa, Peru. *Geological Society of America Bulletin*, 113(12), 1593-1610.

Tierz, P., Sandri, L., Costa, A., Sulpizio, R., Zaccarelli, L., Di Vito, M., and Marzocchi, W. (2016a). Uncertainty assessment of pyroclastic density currents at Mount Vesuvius (Italy) simulated through the energy cone model. Natural Hazard Uncertainty Assessment: Modeling and Decision Support, 223, 125-145.

Tierz, P., Sandri, L., Costa, A., Zaccarelli, L., Di Vito, M., Sulpizio, R., and Marzocchi, W. (2016b). Suitability of energy cone for probabilistic volcanic hazard assessment: validation tests at Somma-Vesuvius and Campi Flegrei (Italy). *Bulletin of Volcanology*, 78(11), 79.

Todesco, M., Neri, A., Esposti Ongaro, T., Papale, P. and Rosi, M. (2006). Pyroclastic flow dynamics and hazard in a caldera setting: Application to Phlegrean Fields (Italy). *Geochemistry, Geophysics, Geosystems*, 7(11).

Voight, B., Constantine, E., Siswowidjoyo, S., and Torley, R. (2000). Historical eruptions of Merapi volcano, central Java, Indonesia, 1768–1998. *Journal of Volcanology and Geothermal Research*, 100(1-4), 69-138.

Voight, B., and Davis, M. (2000). Emplacement temperatures of the November 22, 1994 nuée ardente deposits, Merapi Volcano, Java. *Journal of Volcanology and Geothermal Research*, 100(1-4), 371-377.

Wadge, G., and Isaacs, M. (1988). Mapping the volcanic hazards from Soufriere Hills Volcano, Montserrat, West Indies using an image processor. *Journal of the Geological Society*, 145(4), 541-551.

Walker, G. P. (1983). Ignimbrite types and ignimbrite problems. *Journal of Volcanology and Geothermal Research*, 17(1-4), 65-88.

Worni, R., Huggel, C., Stoffel, M., and Pulgarín, B. (2012). Challenges of modeling current very large lahars at Nevado del Huila Volcano, Colombia. *Bulletin of Volcanology*, 74(2), 309-324.

Yang, Q., Pitman, E., Spiller, E., Bursik, M., and Bevilacqua, A. (2020). Novel statistical emulator construction for volcanic ash transport model Ash3d with physically motivated measures. *Proceedings of the Royal Society A*, 476(2242), 20200161.

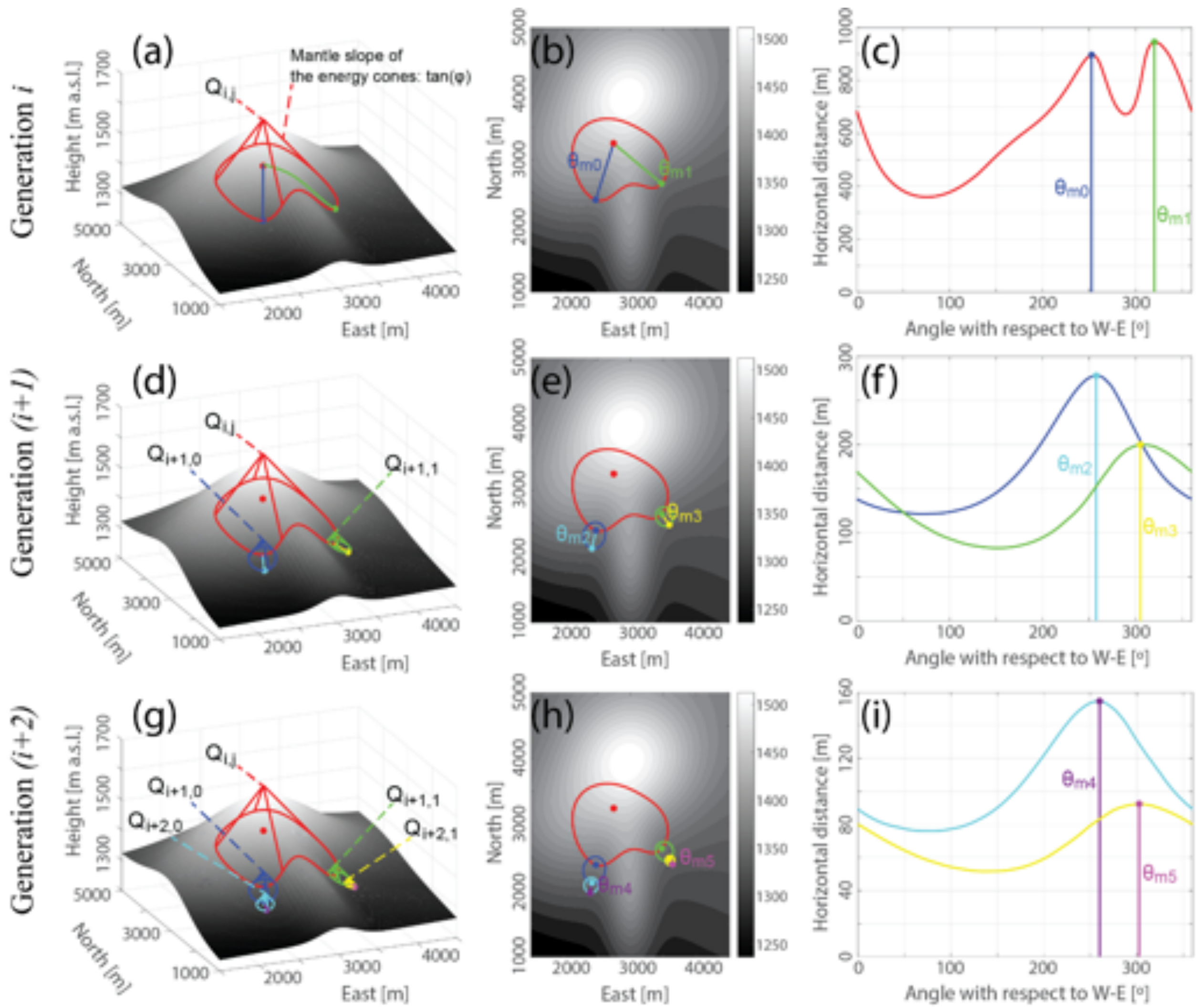

Figure 1. Illustrative example of the tree-like structure used in the branching energy cone model. More details can be found in Aravena et al. (2020). Left-hand side: surface plots of the energy cones and the topography. Central column: contour plots of the energy cones and the topography. Right-hand side: functions of horizontal distance (i.e. run-out distance as a function of the polar angle) of the different generations of energy cones. The number of generations increases from top to bottom.

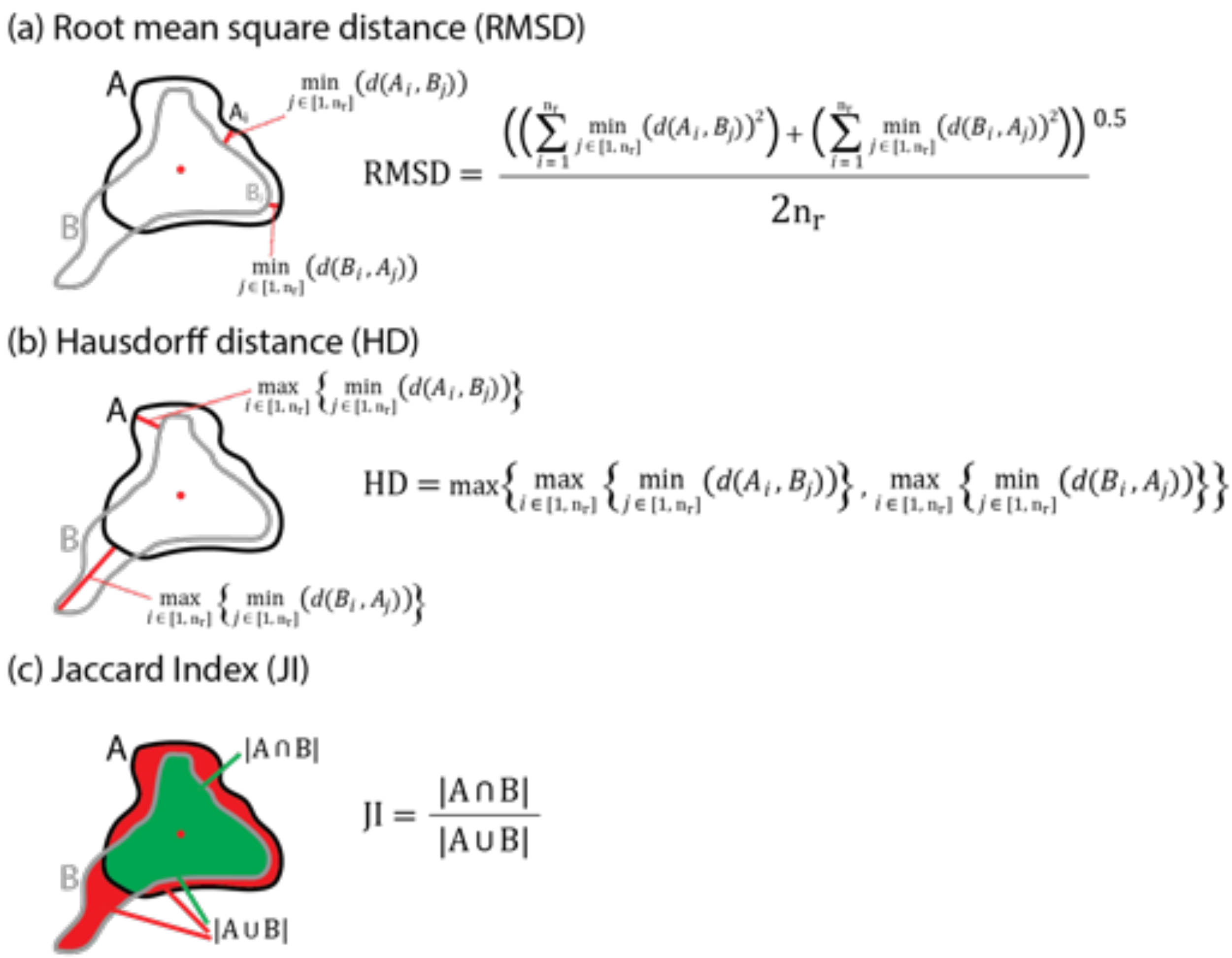

Figure 2. Illustrations of the different metrics used to calculate the similarity index between a reference scenario, defined by the reference inundation polygon A, and a given calibration simulation characterized by the inundation polygon B (see Section 3.1).

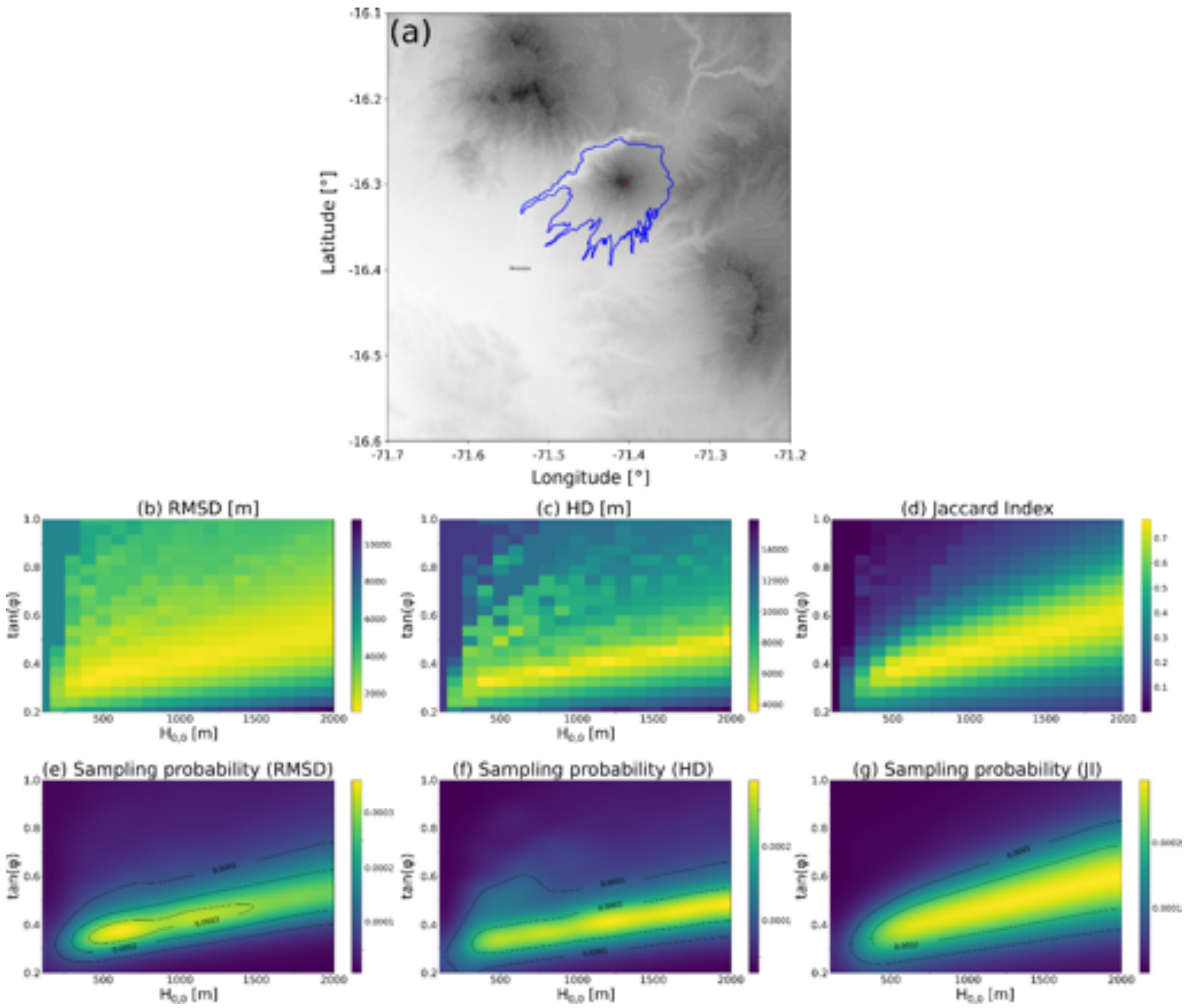

Figure 3. (a) Elevation map of El Misti volcano (Peru) including the PDC inundation area associated with the 2070 cal yr BP eruption (Charbonnier et al., 2020), used to calibrate the branching energy cone model. The red point represents the collapse position used in the calibration simulations. These simulations took ~170 min on an Intel Core i5-2320 CPU at 3.00 GHz (~25 s per simulation). (b-d) Pseudo-color plots of the different coincidence parameters (RMSD, HD and JI) computed from the calibration simulations. In these panels, yellow pixels are associated with high similarity indexes between the calibration simulations and the reference inundation polygon, and blue pixels indicate low degrees of similarity between the computed invasion zones in the calibration simulations and the reference inundation polygon. (e-g) Sampling probability distributions of input parameters ($H_{0,0}$ and $\tan(\varphi)$) used in different sets of simulations for El Misti volcano (see Fig. 4), which derive from the calibrations simulations displayed in panels b-d.

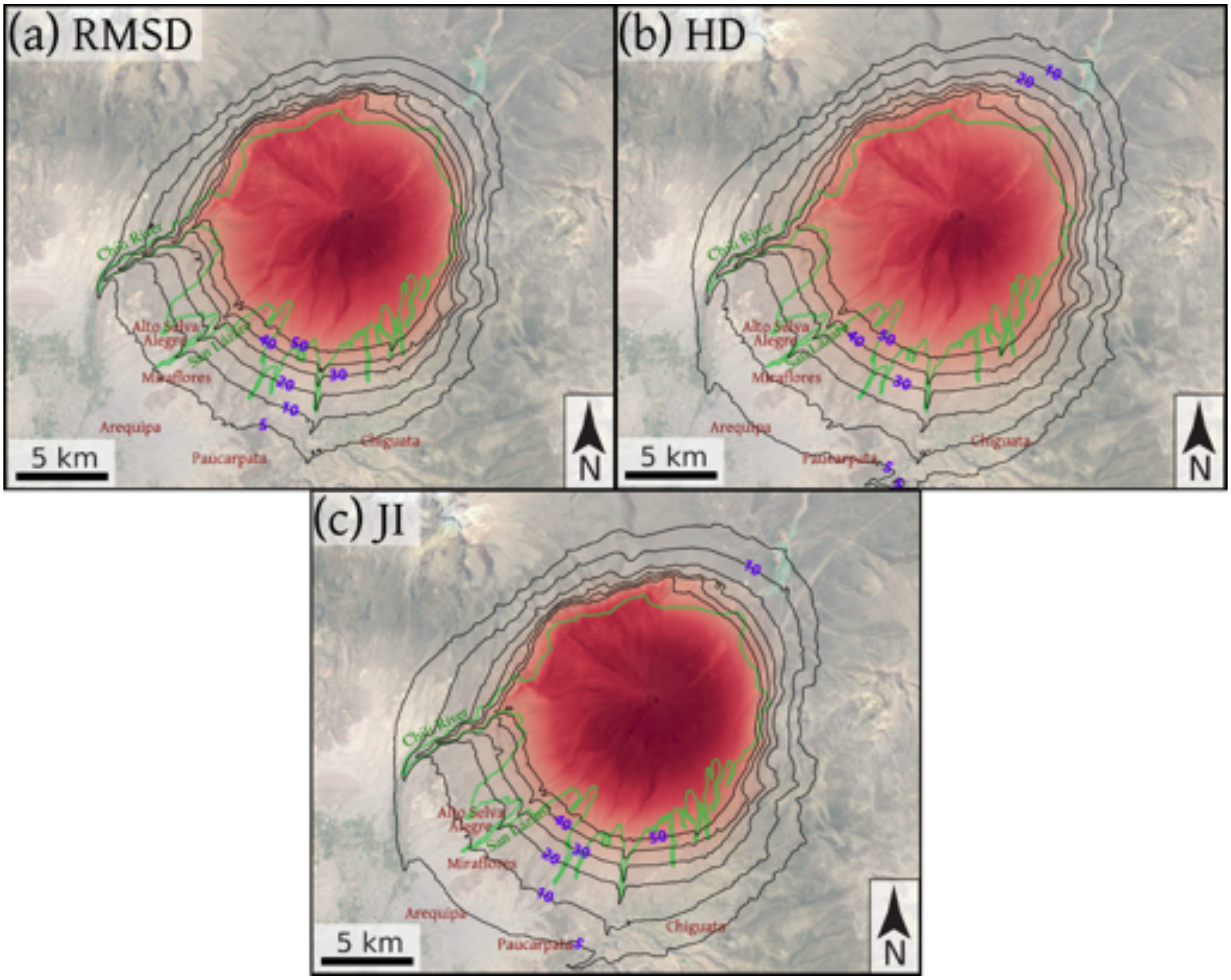

Figure 4. Maps of PDC inundation probability at El Misti volcano imported in a GIS environment. Results are expressed in percent. Each set of simulations took ~480 min on an Intel Core i5-2320 CPU at 3.00 GHz (~29 s per simulation). The input parameters used in these simulations derive from the calibrations displayed in Figure 3. The reference PDC deposit used for the numerical calibration of input parameters is displayed in green (2070 cal yr BP eruption; Charbonnier et al., 2020).

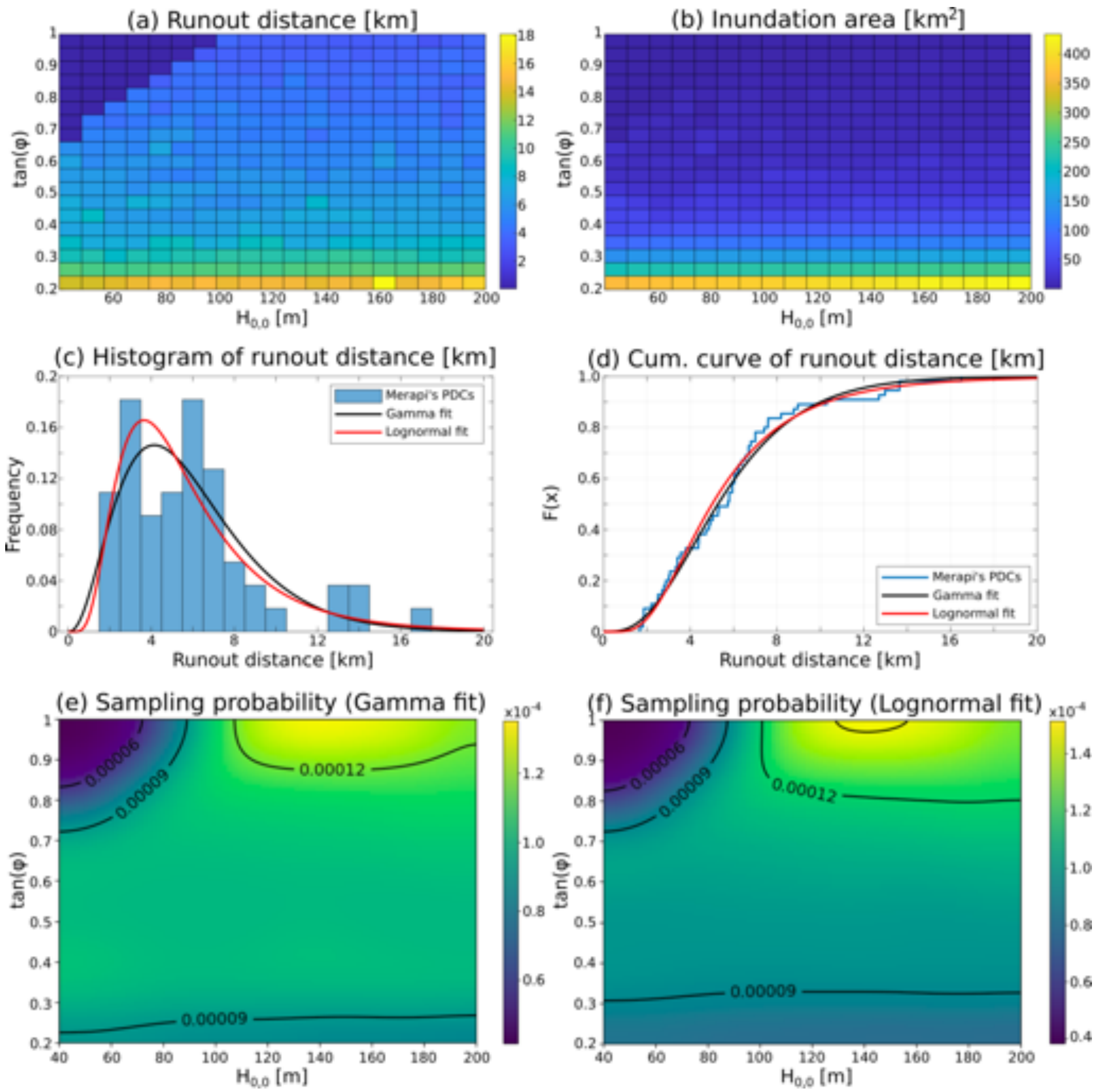

Figure 5. (a-b) Pseudo-color plots of runout distance and inundation area derived from the set of calibration simulations performed for Merapi volcano. These calibration simulations took ~140 min on an Intel Core i5-2320 CPU at 3.00 GHz (~21 s per simulation). (c-d) PDF and CDF of the predefined probability distributions of runout distance used for the calibration of input parameters used in Merapi simulations. These distributions derive from fitting the data of 55 PDCs (Solikhin, 2015), which is displayed as a histogram (c) and an empirical cumulative curve (d), using gamma and lognormal probability distributions. (e-f) Sampling probability distribution of input parameters (collapse height and $\tan(\varphi)$) used in two sets of simulations performed for Merapi volcano (see Fig. 6).

1012

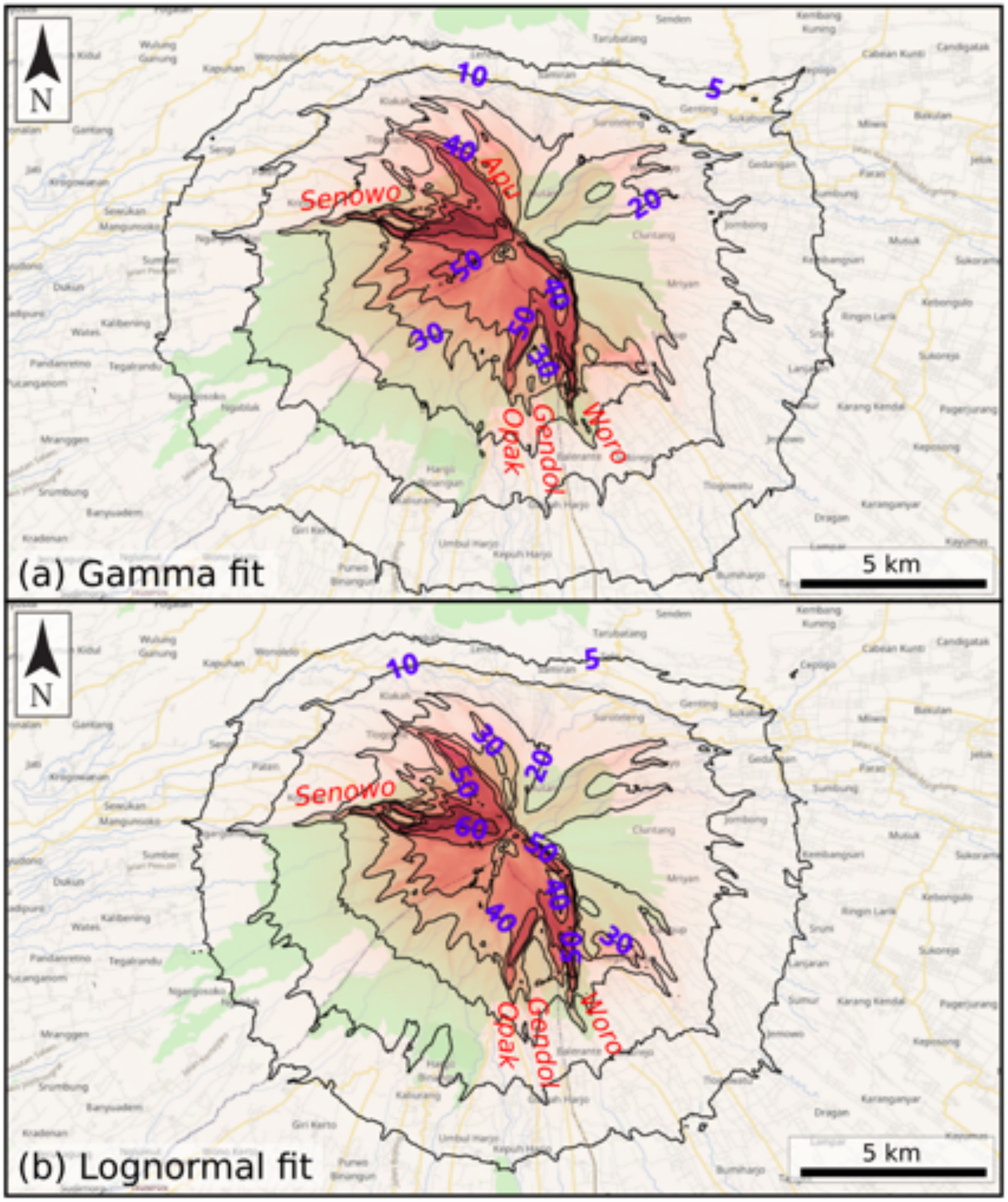

Figure 6. Probability maps of PDC inundation at Merapi volcano constructed using the branching energy cone model. Collapse positions were sampled uniformly within a 300 m-radius circle in the volcanic summit while collapse parameters (i.e. collapse height and $\tan(\varphi)$) were sampled considering the distribution of runout distance observed in the geological record (Solikhin, 2015). This data was fitted using gamma (a) and lognormal (b) probability distributions (Fig. 5c-f). Each set of simulations took ~120 min on an Intel Core i5-2320 CPU at 3.00 GHz (~14 s per simulation). Results are expressed in percent.

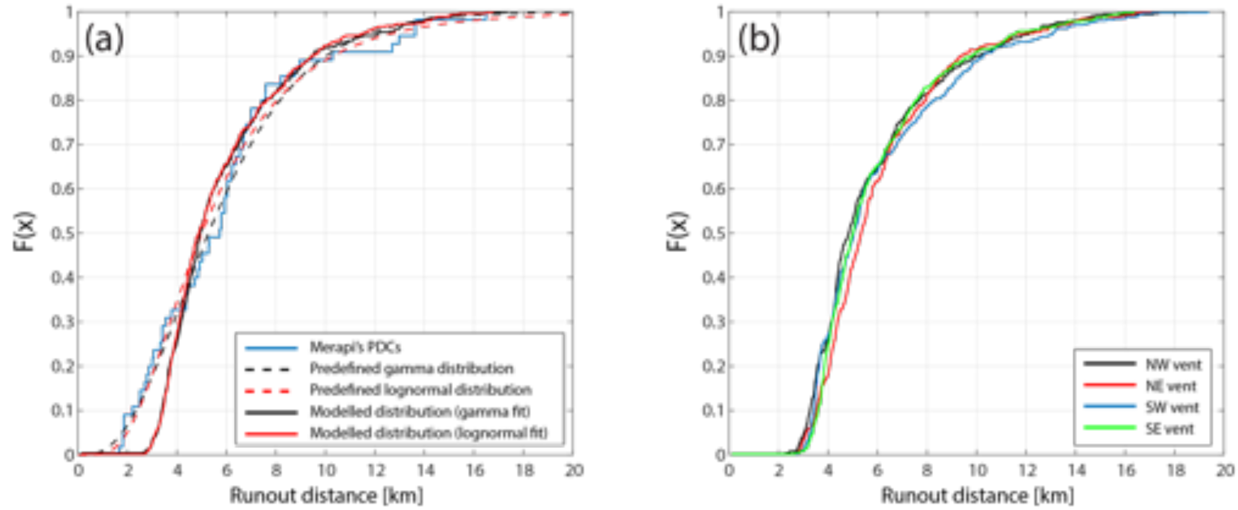

Figure 7. (a) Empirical cumulative curves of runout distance in documented PDCs at Merapi and in the simulation sets presented in Figure 6. The predefined probability functions of runout distance, derived from fitting the data of documented PDCs (Solikhin, 2015) using both gamma and lognormal probability functions, are included. The differences between these curves are mainly related to the absence of runout distances lower than 2.5 km in the modeling results. (b) Empirical cumulative curves of runout distance in the simulation sets presented in Figure 8.

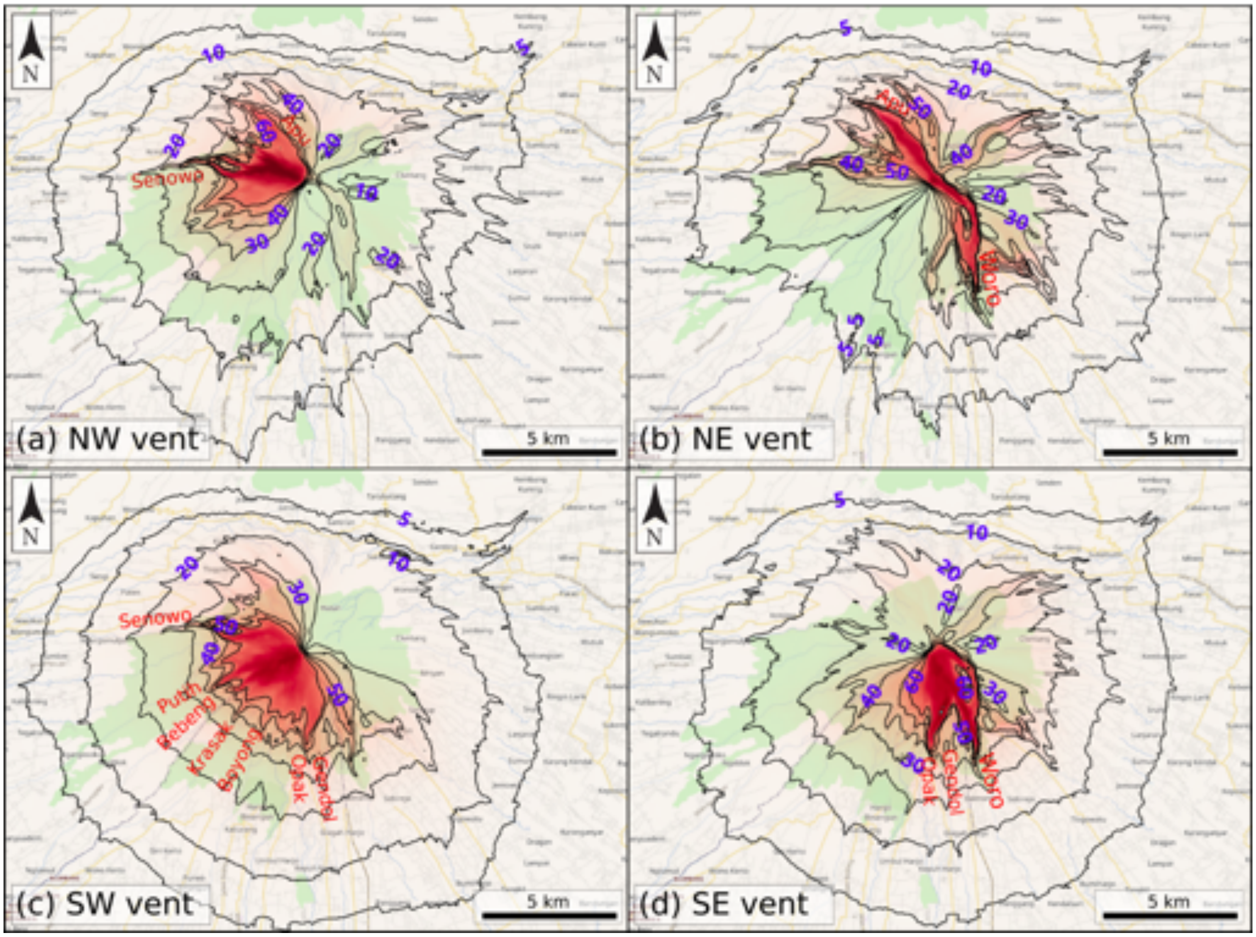

Figure 8. Probability maps of PDC inundation at Merapi volcano considering collapse positions in different flanks of the volcano. These maps were constructed using the branching energy cone model. Collapse positions were sampled uniformly within different regions of a 300 m-radius circle centered in the volcano summit. Four regions were considered: NW (a), NE (b), SW (c), and SE (d). Collapse parameters (i.e. collapse height and $\tan(\varphi)$) were sampled considering the distribution of runout distance observed in the geological record (Solikhin, 2015). This data was fitted using a gamma probability distribution (Fig. 5c, e). Results are expressed in percent.

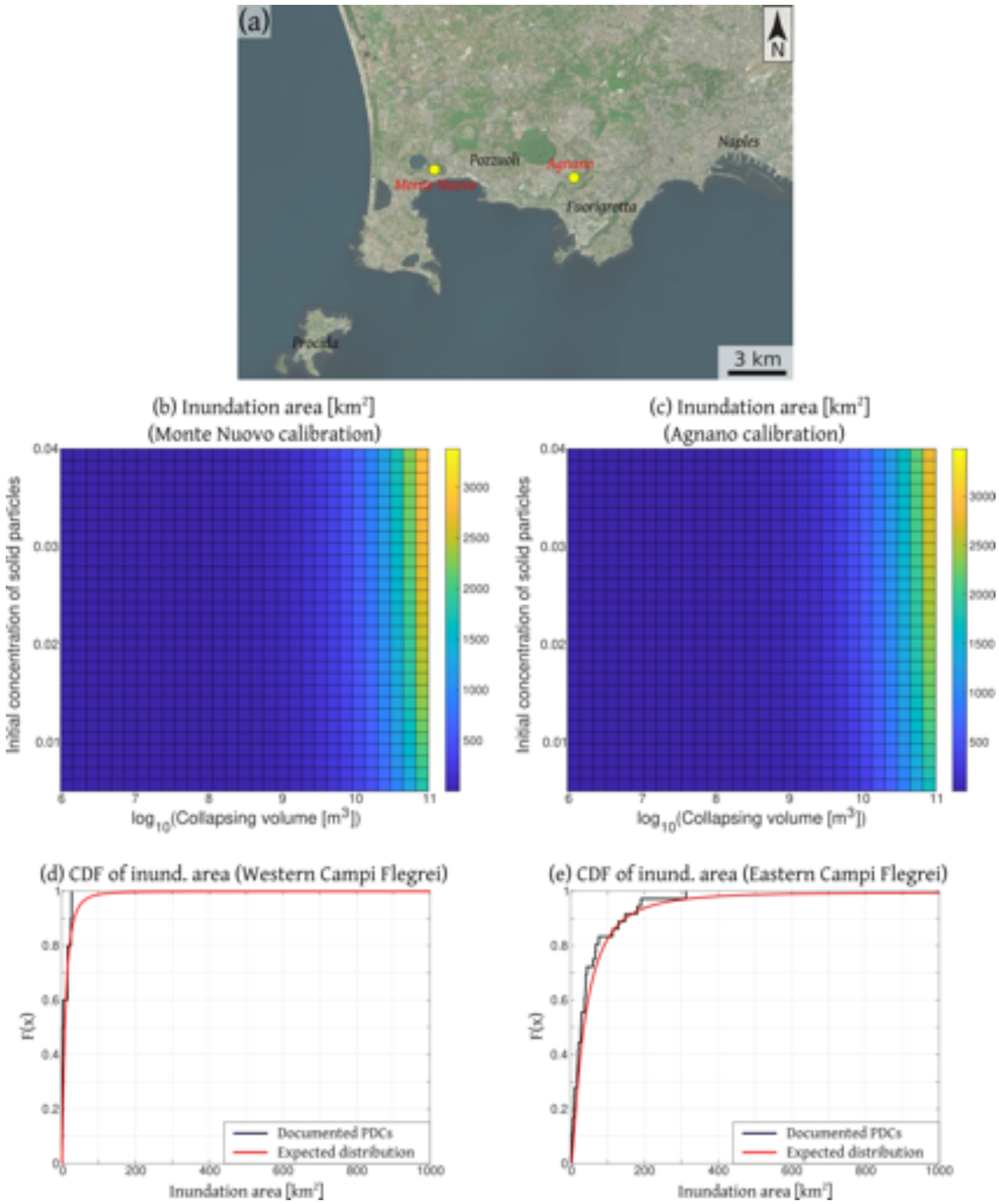

Figure 9. (a) Map of Campi Flegrei showing the points used as the collapse position in the calibration simulations. (b-c) Pseudo-color plots of inundation area derived from the set of calibration simulations performed for Campi Flegrei. (d-e) CDFs of the inundation area in documented PDCs at the western and eastern domains of Campi Flegrei and the expected probability distributions of this parameter, computed following Neri et al. (2015) and Bevilacqua et al. (2017) in order to consider the effect of eventual underestimations of the area of PDC deposits and the presence of "lost" deposits in the dataset.

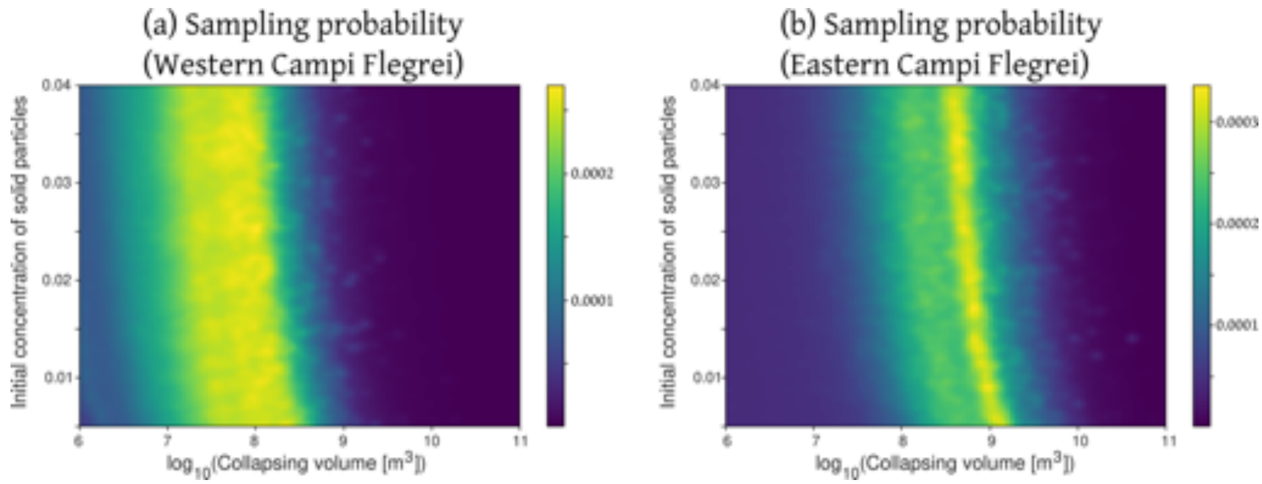

Figure 10. Sampling probability distributions of input parameters (collapsing volume and initial concentration of solid particles) in two sets of simulations performed for Campi Flegrei (see Fig. 11).

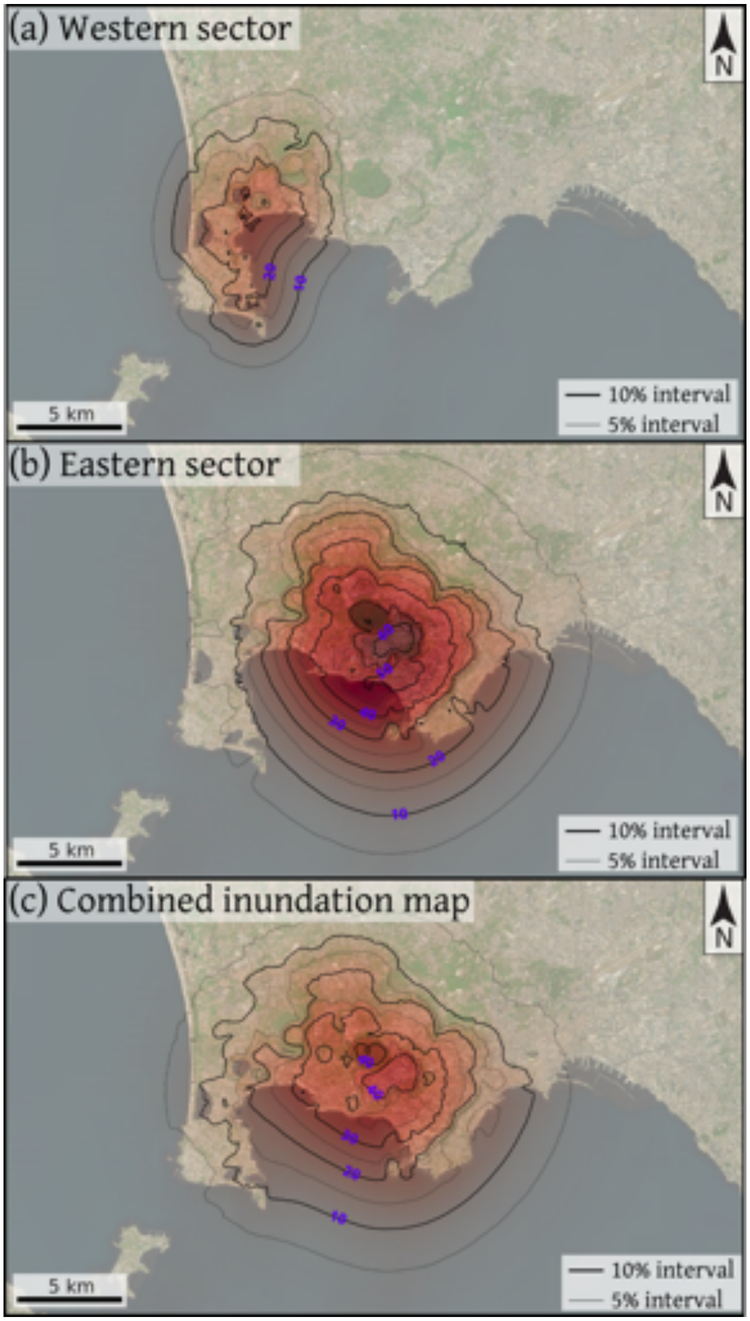

Figure 11. Probability maps of PDC inundation at Campi Flegrei constructed using the traditional box model. Collapse positions were sampled from published vent opening probability maps (Neri et al, 2015; Bevilacqua et al., 2017), while the other model inputs were sampled considering calibrations based on the expected distribution of inundation area.

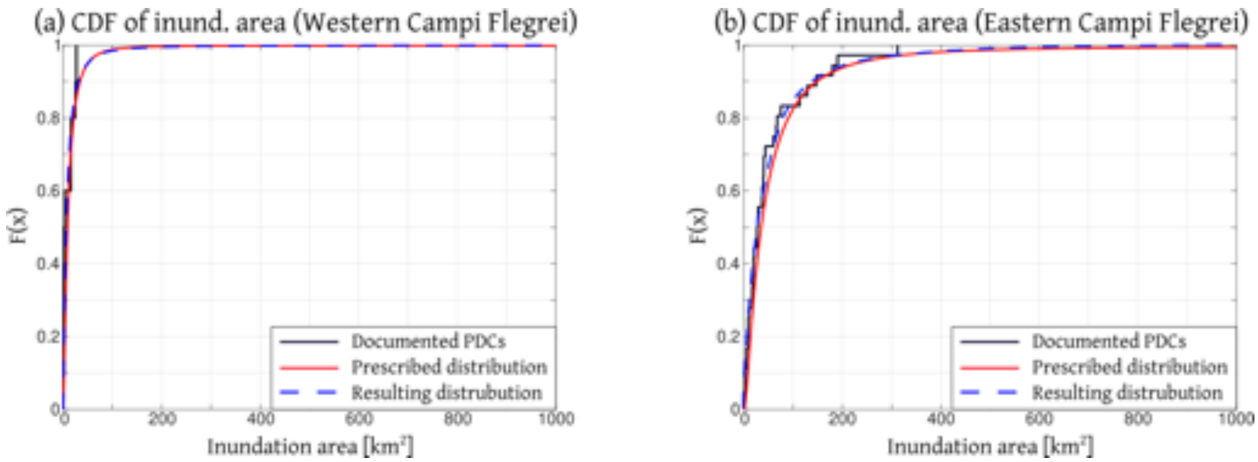

Figure 12. CDFs of the inundation area in documented PDCs at the western and eastern domains of Campi Flegrei, the expected probability distributions of this parameter (i.e. prescribed in our numerical simulations), and the resulting distributions of inundation area in the simulations presented in Figure 11.